

This is a non-peer-reviewed preprint submitted to EarthArXiv.

Please note the manuscript has yet to be formally accepted for publication. Subsequent versions of this manuscript may have slightly different content. If accepted, the final version of this manuscript will be available via the 'Peer-reviewed Publication DOI' link on the right-hand side of this webpage. Please feel free to contact any of the authors; we welcome feedback.

### Direction-dependent permeability and resistivity of fractured rocks tuned to New Zealand geothermal reservoirs

Alison Kirkby<sup>1</sup>, Cécile Massiot<sup>2</sup>

Alison Kirkby<sup>1</sup>, Cécile Massiot<sup>2</sup>

IEarth Sciences New Zealand, Wairakei Research Centre, 114 Karetoto Road, Taupo 3384, New Zealand

IEarth Sciences New Zealand, Avalon Campus, 1 Fairway Drive, Avalon 5011, New Zealand

#### Abstract

11

32

33

- 12 Understanding permeability in the Earth is vital to optimizing sustainable resource
- development such as geothermal. In many geothermal fields, permeability is controlled by
- faults, resulting in high spatial and directional variability, difficult to characterise without
- 15 costly drilling. Electrical resistivity, however, can be measured from the surface, and like
- permeability, is sensitive to fluids if they are sufficiently conductive. Modelling of resistivity-
- based geophysical data has largely focussed on isotropic properties to map clay caps and deep
- heat sources. However, faults commonly have a preferred orientation, and fluid-filled faults
- often have lower resistivity than the matrix, so anisotropy of permeability and resistivity is
- 20 expected. This study models faults from the borehole to field scale to characterise direction-
- 21 dependent permeability and resistivity. Parameters are derived from active faults and
- 22 geothermal fields in the Taupō Volcanic Zone (TVZ), New Zealand. Permeability is highest
- 23  $(1 \times 10^{-12} \text{ m}^2)$  in the horizontal along-dominant-strike direction, lower vertically  $(4 \times 10^{-14} \text{ m}^2)$ ,
- 24 and lowest in the across-dominant strike direction (2×10<sup>-14</sup> m<sup>2</sup>), with significant uncertainty
- 25 in across-strike permeability  $(4 \times 10^{-15} \text{ m}^2 \text{ to } 9 \times 10^{-14} \text{ m}^2)$ . For typical TVZ fluids, resistivity is
- lowest along dominant strike (190  $\Omega$ m), slightly higher vertically (230  $\Omega$ m) and highest
- 27 across-strike ( $465 \pm 30 \ \Omega m$ ). Resistivity anisotropy ratios along-strike/across-strike are
- relatively consistent regardless of fault size distribution (~0.33-0.48). Anisotropy ratios for
- 29 permeability are more variable (1-300). The calculated petrophysical properties provide
- 30 numerical inputs to design geophysical surveys to measure direction-dependent resistivity,
- 31 which may assist with improving fractured reservoir models and resource use.

#### Plain language summary

- 34 Understanding how easily water can move underground (i.e. permeability) is important for
- using resources like groundwater and geothermal in an economic and sustainable way. In
- many geothermal areas, like those in New Zealand's Taupō Volcanic Zone (TVZ),
- 37 permeability is mostly controlled by faults, or cracks, within the Earth. These vary in size and
- 38 direction and can be difficult to find.
- 39 Scientists can measure Earth's electrical resistivity to study geothermal areas and work out
- 40 where to drill with the best chance of finding permeable zones. To simplify these models,
- 41 they normally assume the properties are the same in all directions. However, faults tend to
- 42 line up in certain directions and contain fluids that affect resistivity, both the resistivity and
- 43 the ability of the rock to flow fluids can change depending on the direction they are
- 44 measured.
- 45 This study uses numerical models to look at how faults affect permeability and resistivity at a
- 46 range of scales. The results show that permeability is highest along the main fault direction,
- 47 lower vertically, and lowest across the faults. Resistivity also changes with direction, but less
- 48 dramatically.
- 49 These findings may help better design of geophysical surveys, making it easier to understand
- and manage geothermal resources.

#### 1. Introduction

- 53 Rock permeability is essential for the extraction and recharge of Earth resources such as
- 54 groundwater and geothermal, as well as hydrothermal and volcanic systems. Reservoir
- 55 permeability is often controlled by fractures and faults (McNamara et al. 2015, Bolós et al.
- 2019, Intani et al. 2020, Jolie et al. 2021, Liotta et al. 2021). In these cases, the density, 56
- 57 orientation and connectivity of open faults are key considerations in designing drilling
- strategies to extract fluids. 58
- 59 Resistivity-based geophysical methods such as magnetotellurics (MT) are applied to
- understand geothermal resources. They are highly sensitive to the clay alteration zone that 60
- commonly overlies the reservoir and deep heat sources (e.g., Bibby et al. 1995, Bertrand et al. 61
- 2013, Lee et al. 2020, Ardid et al. 2021, Bertrand et al. 2022, Ishizu et al. 2022, Yamaya et al. 62
- 2022). Key information that is often missing is the distribution and orientation of open 63
- fractures within the reservoir or upflow zone. Interpretation of acoustic and micro-resistivity 64
- borehole images often shows that faults and fractures inferred to be open commonly show a 65
- preferred orientation (e.g. Dezayes et al. 2010, McNamara et al. 2015, Vidal et al. 2016, 66
- Massiot et al. 2017, McNamara et al. 2019, Ikhwan et al. 2020, Milicich et al. 2023). 67
- Reservoir observations (e.g. Calibugan et al. 2022) and discrete fault network models 68
- 69 (Kissling and Massiot 2023) suggest that bulk permeability is also anisotropic. However,
- 70 information on fault orientations, and implications for permeability, is normally not known
- 71 until after several wells have been drilled. Seismic anisotropy has shown promise in
- 72 constraining fault orientations (e.g., Mroczek et al. 2020, Jylhänkangas 2024) although such
- 73 data does not directly image the connectivity of fluids.
- 74 Although resistivity is a direction dependent property, published resistivity models are largely
- 75 isotropic, mainly because the number of parameters to be solved is already far larger than the
- 76 number of data, and in most cases, it is possible to find an isotropic model that has an
- 77 adequate fit to the data. However, electrical resistivity can vary with orientation, both on a
- 78 micro-scale (due to the alignment of mineral grains) and a macro scale (due to bedding or
- 79 aligned faults or faults) (Wannamaker 2005, Martí 2014). In the case of geothermal reservoirs
- 80 containing faults filled with fluids, macro-anisotropy in resistivity may be directly related to
- the alignment of permeable structures. Indeed, fluids are normally more conductive than the 81
- 82 rock matrix. Although conductive clay minerals are abundant in the lower-temperature
- 83 (<200 °C) parts of the hydrothermal system, these generally transition to more resistive clays
- and crystalline minerals at high temperatures (Browne 1970, Muraoka et al. 1998, Simmons 84
- and Browne 2000, Franzson et al. 2008, Jolie et al. 2021). Conductive sulphide minerals such 85
- as pyrite can occur at rates of up to a few percent locally which may influence the host rock 86
- 87 resistivity (Simmons and Browne 2000, Wallis et al. 2009). However, on a field scale, overall
- 88 concentrations tend to be small (1%) limiting the impact of these phases on the overall
- resistivity and particularly any direction dependence of resistivity (Simmons and Browne 89
- 90 2000). Thus, attributes of the resistivity tensor (orientation, and relative magnitude of the
- 91 components) could be a key piece of information in understanding the permeability structure
- 92 of a reservoir controlled by fluid-filled faults.
- 93 The permeability of fractures and faults has been measured on the sub-metre scale (Watanabe
- 94 et al. 2008, Watanabe et al. 2009, Ishibashi et al. 2015, Heap and Kennedy 2016), but there
- 95 are far fewer measurements of fault permeability on the reservoir scale. Instead, bulk
- 96 reservoir permeability is usually determined in the calibration of numerical reservoir models

- 97 (Kaya et al. 2014, Tateishi et al. 2015, O'Sullivan et al. 2025). Resistivity of individual faults
- has been measured, although this is done less often than permeability (Sawayama et al.
- 99 2021a, Sawayama et al. 2023). At the reservoir scale, resistivity is inferred from inversion of
- MT data, although this is typically assumed isotropic, and uncertain due to non-uniqueness,
- particularly in the typical geothermal scenario where a conductive clay cap overlies the
- reservoir, reducing sensitivity to structures below this. Downhole resitivity measurements
- have been limited in geothermal fields and focused on isotropic resistivity (Muraoka et al.
- 104 1998, Wallis et al. 2009, Mortensen et al. 2014), while downhole resistivity anisotropy tools
- are sometimes used in hydrocarbon reservoirs (Hou et al. 2016). Petrophysical modelling has
- the potential to link lab- and reservoir scales, and the evolution of the relationship between
- permeability and resistivity between these two scales.
- This paper aims to link permeability estimated at the core scale to that at reservoir scale, and
- then link these permeability estimates to core and reservoir-scale resistivity. Models of (1)
- individual faults and then (2) fault networks, are constructed using parameters from field data
- in geothermal fields of New Zealand's Taupō Volcanic Zone. A particular focus of the
- resulting models will be the anisotropy in both resistivity and permeability that is expected at
- the reservoir scale.

#### 2. Background

#### 115 2.1 Models of fault permeability and resistivity

- Numerical modelling shows resistivity and permeability faults and fault networks display a
- percolation threshold, i.e., both properties are low at small apertures and then change over
- many orders of magnitude at a point when the faults become fully connected through the
- domain (Bahr 1997, Kirkby et al. 2016, Kirkby and Heinson 2017, Kissling and Massiot
- 120 2023). However, the increase in connectivity with increasing volume fraction is normally
- more gradual for resistivity than it is for resistivity, reflecting a less sharply defined
- percolation threshold (Kirkby et al. 2016, Kirkby and Heinson 2017).
- Laboratory measurements of individual faults at variable normal stresses are consistent with
- permeability and resistivity at or just above the percolation threshold, with permeability on
- individual faults typically around  $10^{-12}$  to  $10^{-13}$  m<sup>2</sup> on faults with no displacement, and  $10^{-9}$  to
- 126 10<sup>-8</sup> m<sup>2</sup> on faults with 3-5 mm displacement (Watanabe et al. 2008, Watanabe et al. 2009,
- 127 Ishibashi et al. 2015, Sawayama et al. 2023).
- The fraction of these measured faults that has both planes in contact covers a relatively
- narrow range of 35-42% for faults with >1 mm displacement, which is near constant with
- pressure, at pressures from 10-100 MPa (Watanabe et al. 2008, Watanabe et al. 2009,
- 131 Ishibashi et al. 2015). For faults with 0-1 mm displacement, contact areas increase more
- strongly with pressure from 31-66%. Thus, faults should be modelled with realistic contact
- area ratio to produce realistic fracture properties.
- 134 A challenge of modelling fault flow properties is balancing small cell sizes needed to capture
- fluid flow effects of sub-mm scale fault roughness against modelling large enough
- areas/volumes to represent the scale of interest. Due to the minimum cell sizes of <1mm
- needed to model fault roughness, the typical scale of simulation is limited to tens of cm to
- metre-scale (Ishibashi et al. 2015, Kirkby et al. 2016, Kirkby and Heinson 2017, Sawayama
- et al. 2021a). However, estimating resistivity and permeability at the scale of a geothermal

- reservoir requires faults at scales of centimetres to tens of metres or more. While fault size,
- on its own, does not impact resistivity and permeability (Ishibashi et al. 2015, Sawayama et
- al. 2023), the displacement on faults increases with fault size (Kim & Sanderson 2005). For
- normal faults, this increase is broadly linear on a log scale, with slope  $\sim 1$ ; i.e., displacement
- is a constant fraction of size (Kim and Sanderson 2005). As displacement on a fault grows,
- opposing surfaces become increasingly mismatched, leading to an increase in the size of
- asperities on the fault, increased space for fluids and thus an increase in permeability and
- decrease in resistivity (Sawayama et al. 2023). These larger asperities are likely to dominate
- both current and fluid transport properties over any fine scale roughness caused by sub-mm
- scale mismatching on the fault planes, allowing cell size to be increased for larger faults with
- larger displacements (Section S1).

#### 2.2 Taupō Volcanic Zone

- To focus this study, and enable direct comparison to observations, model parameters were
- selected based on characteristics of the Taupō Volcanic Zone (TVZ), New Zealand (Figure 1),
- that has been extensively studied. The TVZ has been the site of geothermal energy production
- 155 for electricity for >50 years and currently provides nearly 20 % of New Zealand's electricity
- 156 (MBIE 2025). The TVZ is Hikurangi Subduction Zone's volcanic arc (Wilson et al. 1995).
- 157 The Taupō Rift is an intra-arc rift where the extension coincides with the TVZ (Wilson and
- Rowland 2016, Villamor et al. 2017). The modern Taupō Rift is a 15 40km wide zone of
- closely spaced faults, dominated by steeply-dipping normal faults (Nicol et al. 2006, Seebeck
- et al. 2014, Villamor et al. 2017, Seebeck et al. 2024, Morgenstern et al. 2025). In geothermal
- fields, numerous studies have characterised fractures and faults using borehole images
- 162 (Wallis et al. 2012, McNamara et al. 2015, Massiot et al. 2017, McNamara et al. 2019,
- Massiot et al. 2023, Milicich et al. 2023, Wallis 2023, Massiot et al. 2025, Morgenstern et al.
- 164 2025), fault systems using stratigraphic offsets (Chambefort et al. 2014, Milicich et al. 2014,
- Rosenberg 2017, Milicich et al. 2020), fluid composition and temperature (Hedenquist 1983,
- Hedenquist 1990, Chambefort et al. 2016, McNamara et al. 2016, Mroczek et al. 2016). In
- addition, electrical resistivity has been measured based on DC resistivity, MT, and airborne
- electromagnetic data (Bibby et al. 1995, Heise et al. 2008, Bertrand et al. 2013, Bertrand et
- al. 2015, Heise et al. 2016, Bertrand et al. 2022, Reeves and Pederson 2023).

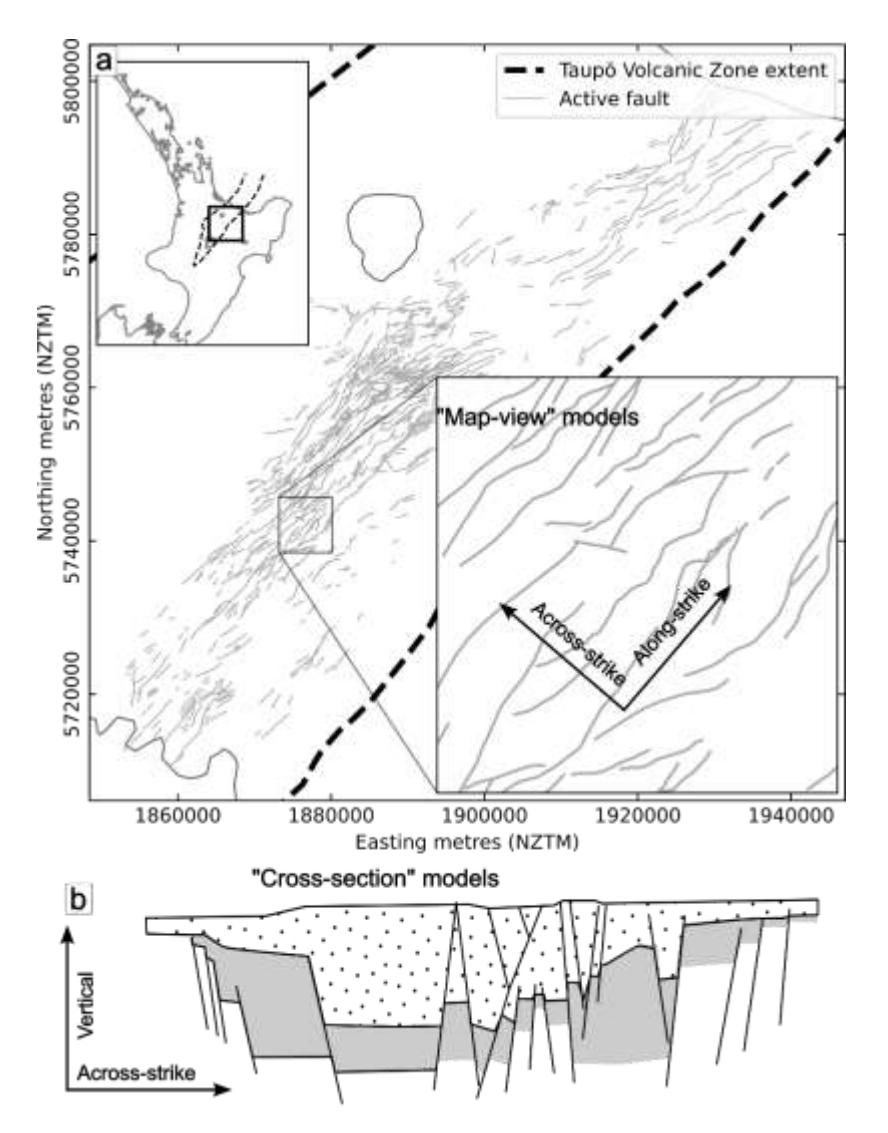


Figure 1. Representative a) map-view and b) cross-section of normal faults antithetic and synthetic splays, that occur in the TVZ from geothermal field to rift scales. Insert of (a) shows the location of the TVZ in the North Island of New Zealand. Active faults after Morgenstern et al. (2025); and TVZ extent after Wilson et al. (1995); the synthetic cross-section is modified after Villamor et al. (2017) and McNamara et al. (2019) and applies to either field- or rift-scales.

#### 3. Method

This study employs a three-stage, 2D approach to first estimate fault resistivity and permeability capturing fine-scale fault roughness (Figure 2), compute resistivity of a small-scale faulted volume, and then upscale to reservoir scale.

#### 3.1 Individual fault models

The first step is to apply the approach of Kirkby et al. (2016) to estimate permeability and resistivity for individual faults of different sizes (Figure 2a-b, f-g), with a modification to the permeability calculation (Section S2). This method generates a pair of synthetic square fault surfaces based on characteristics of real faults (Brown 1995, Matsuki et al. 2006). They are then displaced parallel to the fracture plane by a desired amount (i.e. the top surface is translated along the fault plane). The fault planes are then shifted apart or together until they reach a target percentage of contact area. Regions with overlapping or very small apertures

- are set to a minimum value of 1 μm (Watanabe et al. 2008) to account for sub-μm roughness
- 190 causing asperities at contact points.
- 191 The resistivity and permeability of the faults are then modelled in two directions, parallel and
- 192 perpendicular to the displacement direction. Resistivity and permeability are modelled,
- respectively, by Ohm's law and Darcy's Law using a modified parallel plate method that
- 194 corrects for sloping plates. The models have constant pressure and voltage boundary
- conditions on each end of the fault, and no-flow boundary conditions at the sides (Brown
- 196 1989, Nicholl et al. 1999, Brush and Thomson 2003, Kirkby et al. 2016). This process is
- carried out in faults with thirteen displacement values, ranging from zero to 50 cm
- 198 (approximately evenly in log space), later linked to fault length (Section 3.3.1). For each
- fault, the opposing surfaces are progressively shifted apart and modelled at 30 unique
- proportions of contact area (0.10 to 0.68), with 96 repeats for each displacement value. From
- these models, a subset was selected that were within the range of contact area as discussed in
- 202 Section 3.3.1.
- 203 The resulting fault permeability and resistivity values for each model are provided in both
- directions, i.e. perpendicular and parallel to displacement. Fault resistivity is defined here as
- 205 the equivalent resistivity of a hypothetical, uniformly thick sheet that represent the actual
- fault (Figure 2c-d, h-i). The sheet has a constant width equal to the mean aperture of the fault,
- and its resistivity is computed such that it preserves the same overall electrical response as
- the original fault.
- 209 To pass the resulting permeability and resistivity distributions through to models of a faulted
- volume, the resistivity and hydraulic aperture of the equivalent "sheet" is translated to its
- cross-sectional equivalent, a "fault stick" (Figure 2d, j). This allows fault resistivities to be
- 212 passed into macro-scale models of faulted volumes, as uniformly thick sticks. The parameters
- used for the models are discussed in Section 3.3.

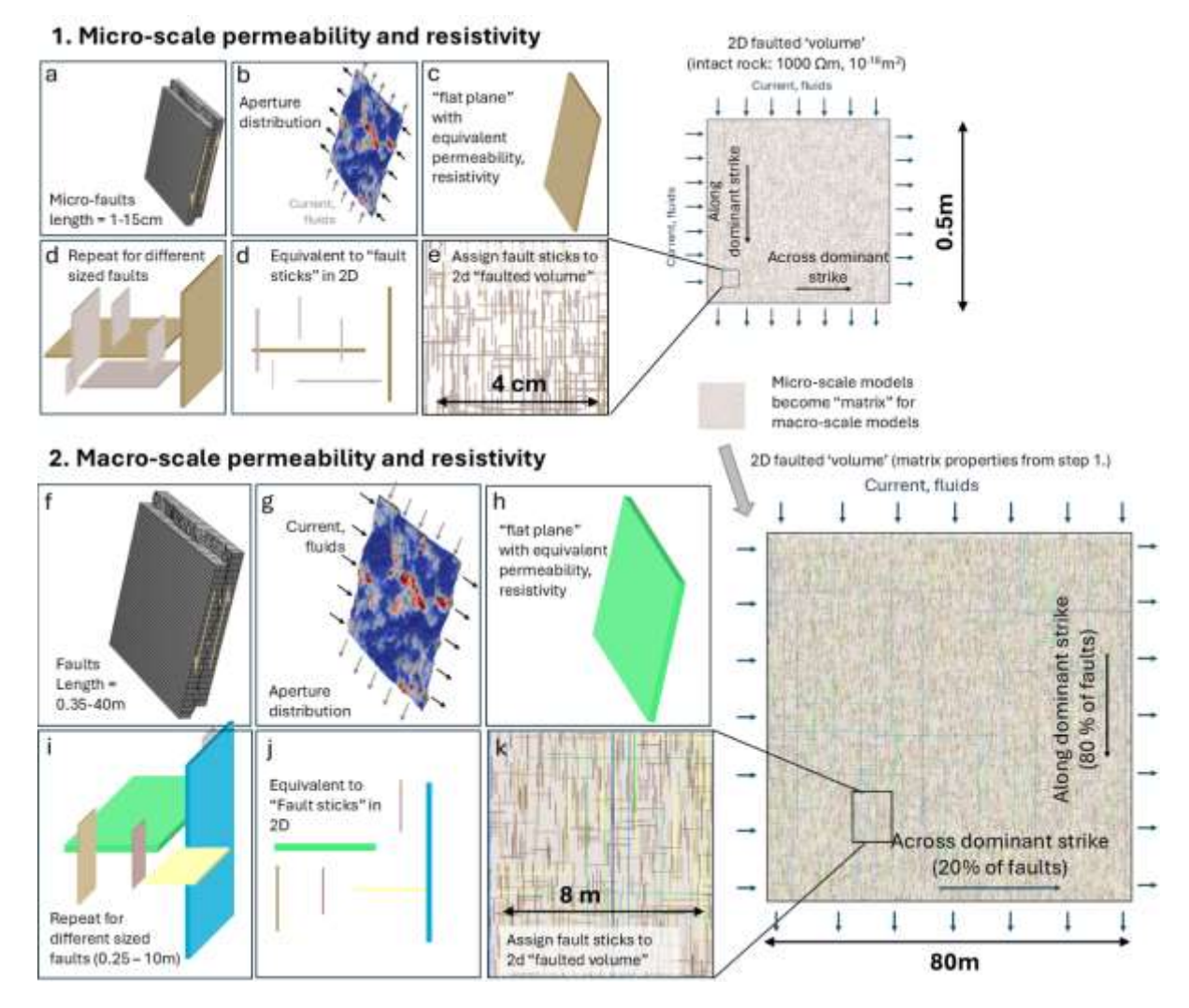


Figure 2. Diagram illustrating the multi-scale approach employed in this study to model the permeability of a faulted volume. The 2d "fault volume" models represent a map-view, when considering a TVZ-like (extensional) regime, with vertical fault displacement and the dominant strike along the rift axis. Explain a-k

#### 3.2 Fault stick models

Individual fault permeabilities and resistivities are then used in 2D "fault stick" models (Kissling and Massiot 2023) (Figure 2). The fault sticks are placed in one of two orthogonal directions. Fault hydraulic aperture and resistivity values are assigned using the results of step (1) (Section 3.1). In these models, the relative proportions of faults of different sizes, and proportions in the direction along the dominant strike direction (P<sub>z</sub>), are set based on field measurements (Section 3.3; Table 1). The models predict bulk permeabilities and resistivity in two directions.

Fault stick models are generated on two embedded scales: first,  $0.5m \times 0.5m$  models, containing faults  $\leq 0.2$  m in length, are used to assess permeability, porosity and resistivity associated with small-scale faults. These are termed "micro-faults". Next, models  $80 \text{ m} \times 80 \text{ m}$  in area were constructed containing faults from 0.3 to 50 m in length. The matrix properties in these models was set as permeability and resistivity from the smaller scale models (Figure 2).

As a 3-dimensional proxy, two sets of 2-D fault stick models were generated. In the first set ("map view") (Figure 1), fault permeabilities and resistivities are defined using individual-

- fault models (Section 3.1) where these properties were modelled perpendicular to slip. In a
- 235 "TVZ-like" regime, dominated by near-vertical normal faults(e.g. McNamara et al. 2019), the
- 236 two directions are horizontal, aligned along the dominant strike (NE-SW) and across the
- dominant strike (NW-SE). We herein refer to these directions as "along-strike" and "across-
- 238 strike". In the second set of models ("cross-section view"), fault permeabilities and
- 239 resistivities parallel to slip were used. These are representative of vertical cross-sections
- oriented NW-SE, i.e. comprising a majority of vertical faults and a minority of horizontal
- 241 faults. The two directions are "vertical" and horizontal across the dominant fault strike
- 242 ("across-strike"). This second set is similar to models of Kissling and Massiot (2023).
- 243 The two "across-strike" models represent the same direction (NW-SE) but will have different
- permeabilities, due to using fault permeability parallel to slip in the "cross-section view"
- 245 models and perpendicular to slip in the "map-view" models. This discrepancy could be
- addressed by modelling fault volumes in 3D. The permeability in the direction across the
- dominant strike will likely be intermediate between the two models and will depend on the
- true direction of fault displacement.

#### 249 3.3 Parameter selection

250

#### 3.3.1 Models of individual faults

- 251 The displacement magnitude on individual faults was scaled with fault length using constant
- 252 fraction of 0.01 (Kim and Sanderson 2005), with faults smaller than 0.1 m assumed to have
- 253 no displacement. This generates asperities that increase in size with fault length. Models had
- a minimum fault length of 1 cm, and a maximum length of 50 m, i.e. 0.5 m displacement. The
- 255 upper limit to scale is driven by the assumption of no deformation/gouge formation on the
- 256 fault plane, which is likely to become invalid for larger fault displacements.
- 257 The roughness of fault surfaces can be characterised by an amplitude parameter and fractal
- dimension D, which controls the relative roughness on a large to small scale (Brown 1995).
- 259 Amplitude of surface heights can be defined in terms of scaling factor s, which relates the
- standard deviation of surface heights of a reference fault,  $\sigma_{h,ref}$  to its length  $L_{ref}$  and fractal
- dimension D (Matsuki et al. 2006, Kirkby et al. 2016):

262 
$$s = \frac{\sigma_{h,ref}}{L_{ref}^{3-D}}$$
 (Equation 1)

- 263 Increasing fractal dimension has minimal effect on flow and resistivity, while increasing
- scaling factor increases permeability and reduces resistivity (Sawayama et al. 2023).
- Measurements on core samples on a variety of lithologies suggest natural faults tend to have
- lower scaling factors, and slightly higher fractal dimensions, than induced faults created in
- 267 the lab (Figure 3), which may reflect deformation on the fault plane during the natural
- 268 fracture generation and slip process. Based on these measurements, we set D=2.34 and
- 269 s=0.0017.

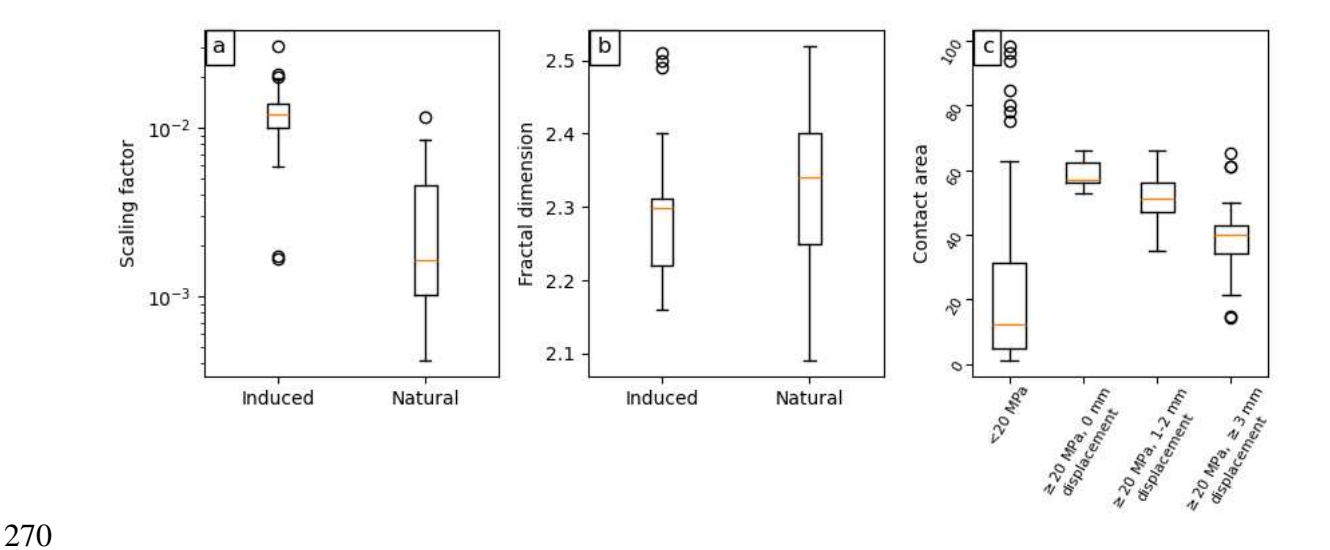


Figure 3. Box and whisker plots of published data for (a) scaling factor, (b) fractal dimension, and (c) contact area proportion on faults and fault surfaces. The orange bars represent the median, and the boxes show the range from the 1<sup>st</sup> to 3<sup>rd</sup> quartile. The whiskers are shown at the furthest data point lying within 1.5 times the interquartile range from the box, with points outside that range shown as circles. Data from (a) and (b) from the following sources: (Brown and Scholz 1986, Chen and Spetzler 1993, Olsson and Brown 1993, Brown 1995, Matsuki et al. 2006, Candela et al. 2012, Ishibashi et al. 2015, Sawayama et al. 2021a, Sawayama et al. 2021b). Data in (c) from: (Sharifzadeh et al. 2008, Watanabe et al. 2008, Nemoto et al. 2009, Watanabe et al. 2009, Ishibashi et al. 2015, Fathi et al. 2016, Wenning et al. 2019). The contact area ranges in Table 1 are the 25<sup>th</sup>-75<sup>th</sup> percentile in (c), i.e. the extent of the boxes for measurements at ≥20 MPa.

Ranges for percentage contact area between fault planes were chosen based on the  $25^{th}$  and  $75^{th}$  percentile from measurements at 20 to 100 MPa (Watanabe et al. 2008, Nemoto et al. 2009, Watanabe et al. 2009, Ishibashi et al. 2015) (Figure 3C). This corresponds to 56-63 % for faults with zero displacement, 47-56% for those with 1-2 mm displacement and 34-43 % for  $\geq$ 3 mm displacement (Watanabe et al. 2008, Nemoto et al. 2009, Watanabe et al. 2009, Ishibashi et al. 2015).

Fluid resistivity is estimated from salinity and temperature. The resistivity of water decreases with increasing temperature and concentration of dissolved ions (e.g. Bannard 1975, Ucok et al. 1980, Watanabe et al. 2022). A representative NaCl content of 2000 ppm was estimated based on estimates of parent fluid Cl<sup>-</sup> concentration ranging from 1069 – 1400 ppm at Ngatamariki, Ohaaki, and Rotokawa geothermal fields in the TVZ (Hedenquist 1983, Hedenquist 1990, Chambefort et al. 2016, Mroczek et al. 2016). This concentration with a reservoir temperature of 280 °C (Chambefort et al. 2016, McNamara et al. 2016, Mroczek et al. 2016) gives a fluid resistivity of  $\sim 0.5 \ \Omega m$  (Watanabe et al. 2022). To explore the changes in bulk resistivity as fluid resistivity is changed, several additional fluid resistivities were considered, ranging from 0.01 to 500  $\Omega$ m. Intact rock (matrix) resistivity is set to 1000  $\Omega$ m.

#### 3.3.2 Fault network parameters

The density of different sized faults can be described by a power law distribution (Bonnet et al. 2001), with the number of faults greater than a given size  $(N_f)$  given in terms of a density constant  $\alpha$  and exponent  $\gamma$ :

300 
$$N_f = \frac{\alpha}{1-\gamma} l_{min}^{1-\gamma} R^2$$
 (Equation 2)

 $\overline{271}$ 

- Here, the exponent was determined based on analysis of a vein dataset collected on exposed
- 302 basement rocks like those found in the deep TVZ (Massiot et al. 2025), with a best fit value
- of 3.1 (Section S3). A similar analysis on the active fault database in the TVZ gives a value of
- 3.6. Since the outcrop dataset is at a more similar scale to our models, we use a base case
- scenario of  $\gamma$ =3.1 but model a range of values (Table 1) to accommodate uncertainties in the
- 306 outcrop dataset.
- 307 If  $\gamma$  and the aperture/volume of each fault is known, then the density constant  $\alpha$  and the fault
- 308 porosity are directly linked, i.e. choice of one parameter implies the other. In measured fault
- 309 systems,  $\alpha$  spans seven orders of magnitude (Bonnet et al. 2001).
- The fracture porosity in natural geothermal systems in the TVZ has been inferred at several
- scales of observation. Borehole images at the Rotokawa and Kawerau geothermal fields
- 312 suggest a porosity of around 4-10 % including large faults, open fractures and filled veins
- 313 (Massiot et al. 2017). A similar combined vein and fracture connected porosity (4-10%) was
- found in thin sections (Siratovich et al. 2014, Wyering et al. 2014, Cant et al. 2018).
- 315 Therefore, the open fault connected porosity is <4-10%. Microscale fault network models
- result in a connected porosity from open faults of ~2 % at the percolation threshold (Kirkby
- and Heinson 2017). Similar estimations of open fracture porosity were found through
- 318 synthetic forward modelling of open faults to match seismic anisotropy responses (2.5 % and
- 319 4.5 % respectively, for the Ngatamariki and Rotokawa geothermal fields) (Jylhänkangas
- 320 2024). Models presented here therefore include a base scenario (2%) and two additional
- 321 scenarios for open fault porosity of 1 % and 3 % (Table 1). Higher porosities were trialled but
- 322 gave unrealistically high permeabilities.
- Finally, the proportion of faults in each orthogonal direction was estimated separately for the
- "map-view" and "cross-section" models, both returning ~0.8. This parameter is termed P<sub>z</sub>, i.e.
- 325 the proportion of faults in the dominant strike direction. For the "map view" models, P<sub>z</sub> was
- estimated based on a length-weighted average of the strike-parallel component of fault
- 327 segments from the Taupō Rift in New Zealand's active fault database (Morgenstern et al.
- 328 2025), relative to the total length of faults in this region (Supplementary Section S4).
- For the vertical direction, P<sub>z</sub> was computed using fault and fracture dip magnitudes
- interpreted from borehole images at the Rotokawa and Wairakei geothermal fields (Massiot et
- al. 2017, McNamara et al. 2019). Borehole images do not inform on fault length, so each
- fault was weighted as if it had the same length. Borehole image-derived P<sub>z</sub> is similar to that
- calculated from active faults (0.79). Thus a value of 0.8 was used to define the relative
- proportion of faults along and across the dominant strike, for both the "map view" and
- "cross-section" sets of fault models.

339

- Fault centres and orientations were assigned randomly while matching P<sub>z</sub>. To test the
- sensitivity of the models to P<sub>z</sub>, a range of values was tested from 0.7 to 0.99.

Individual fault parameters											
Base case scenario Single parameter sensitivity and					alysis						
Length (L)	0.01 – 50 m (13 fault lengths). Faults with length < 0.1 m were given same properties as 0.1 m faults.	As base case									
Cell size	L / 500 to a minimum of 0.1 mm	As base case									
Displacement (d)	0.01 x L	As base case									
Fractal dimension	2.34	As base case									
Scaling factor	0.0017	As base case									
Area of contact between fault planes (inter- quartile ranges from Figure 2c)	56-63 % (d = 0 mm) 47-56% (d = 1- 2 mm) 34-43 % (d \ge 3 mm)	As base case									
Fluid resistivity (p <sub>f</sub> )	0.5 Ωm	0.01 to 50									
Matrix resistivity	1000 Ωm	As base case									
Matrix permeability	10 <sup>-18</sup> m <sup>2</sup>	As base case									
Number of repeats	96 for each displacement	As base case									
Fault network parameters											
Cell size	0.5 mm (0.5 m x 0.5m model) 0.05 m (80 m x 80 m model)	As base case									
Fault density exponent (γ)	3.1	2.9	3.0	3.1	3.1	3.2	3.3				
Fracture porosity	2%	2%	2%	1%	3%	2%	2%				
Fault density constant <i>α</i>	3.16	5.80	4.40	1.59	4.73	2.19	1.48				
Proportion along- strike / vertical faults (Pz)	0.8	0.7, 0.8, 0.9, 0.95, 0.98, 0.99, 1.0									
Number of repeats	100 for each parameter set	As base case									

- 343 **4. Results**
- 344 4.1 Properties of individual faults
- 345 4.1.1 Permeability
- Fault permeability distributions, and fault resistivity distributions from three of the modelled
- fluid resistivities are shown in Figure 4. For faults with no displacement, permeability in both
- directions has a strong peak at  $\sim 2 \times 10^{-13}$  m<sup>2</sup>. For faults with 1 mm displacement, permeability
- perpendicular to slip peaks at a lower permeability  $(7 \times 10^{-14} \,\mathrm{m}^2)$ , while fault permeability
- parallel to slip peaks higher  $(4 \times 10^{-13} \text{ m}^2)$ .
- For faults with 2-3 mm displacement, peak permeability is similar to those with 0-1 mm
- displacement, but the distributions have long positive tails. For faults with displacement
- 353 ≥5 mm, the peak in permeability increases with displacement for vertical and along-strike
- directions (Figure 4). This likely reflects larger aperture in these models. The permeability at
- 355 the peak can be predicted reasonably well by a global parallel plate model using the mean
- aperture b and roughness factor  $\beta$ , a multiplier to the physical aperture (Kissling and Massiot
- 357 2023), i.e.
- 358  $k_{peak} = \frac{(\beta b)^2}{12}$  (Equation 5)
- Where  $\beta \approx 0.402$  in the direction perpendicular to slip. The mean aperture b in mm can be
- predicted from displacement, d, to within 1% (for displacement  $\geq 5$  mm) by the expression:
- 361  $b = 0.056 d^{0.668}$  (Equation 6)
- In models parallel to the slip direction, a roughness factor  $\beta$  of 0.185 in Equation 5 can be
- used to predict the position of the main peak. Fitting of Equations 5 and 6 is described in
- Section S5. In these models, there is also a small peak at  $\sim 1 \times 10^{-13}$  m<sup>2</sup> that decreases with
- displacement, suggesting a small proportion of these faults are below their percolation
- 366 threshold.

367

#### 4.1.2 Resistivity

- 368 Fault resistivities show a more compact distribution than permeability, and little variation in
- resistivity with varying length or displacement. This demonstrates that the roughness effect
- on resistivity does not change substantially with displacement. However, the averaged
- resistivity over a constant width (i.e. the resistivity used in the reservoir-scale models)
- decreases with fault displacement, reflecting the increased average aperture associated with
- 373 larger displacement.
- 374 The width of the resistivity histograms is wider (in log-space) for faults filled with lower
- 375 resistivity fluid, compared to those with higher resistivity fluid, reflecting the larger contrast
- in resistivity between the rock and the fluid. Resistivity of faults in the direction parallel to
- displacement is higher than resistivity perpendicular to slip, by a factor of 2 ( $\rho_f = 5 \Omega m$ ) to 3
- 378  $(\rho_f = 0.05 \Omega m)$ .

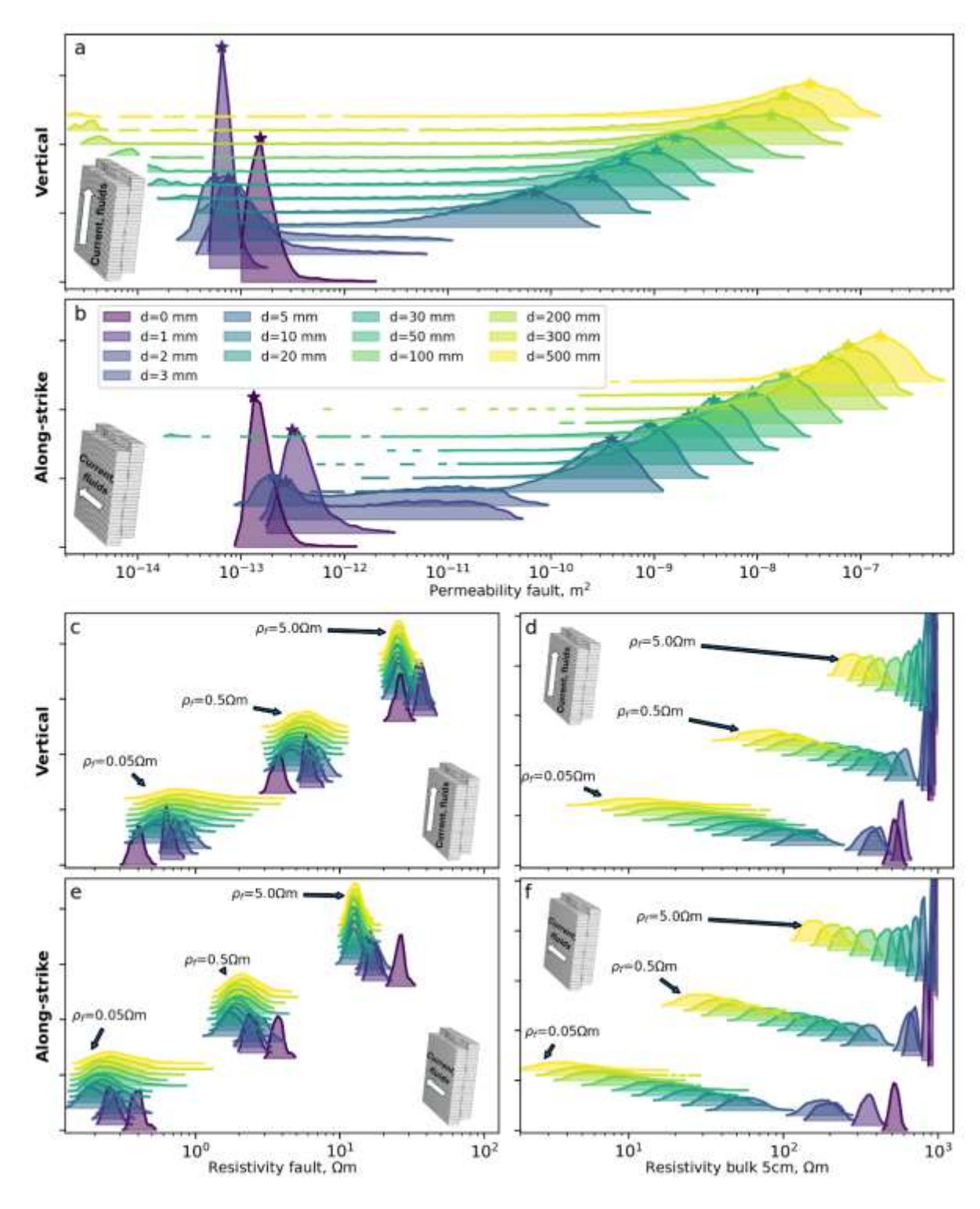


Figure 4. Resistivity and permeability of individual faults from modelling displayed as smoothed histograms, coloured by fault displacement. Histograms are displacement vertically to aid visualisation. (a) and (b): Fault permeability, modelled parallel ("vertical") and perpendicular ("along-strike") to slip direction. (c) and (e): Fault resistivity, modelled parallel ("vertical") and perpendicular ("along-strike") to slip direction. (d) and (f): resistivity of a 5 cm wide model cell containing a fault with displacement D, i.e. these resistivity values form the inputs to the upscaled models. Panels (c) to (f) show resistivity values for faults containing a material with three resistivities ( $\rho_f$ ), as labelled on the figure, i.e. 0.05  $\Omega$ m, 0.5  $\Omega$ m, and 5.0  $\Omega$ m. The stars denote the peak of permeability used to calculate the roughness factor beta (Equation 5; Section S6).

#### 389 4.2 Properties of a faulted volume

- 390 Permeability and resistivity of a faulted volume (base case scenario) are shown in Figure 5.
- 391 Parameter variations are shown in the following four plots; variation with the proportion of
- along-strike or vertical faults  $P_z$  (Figure 6), variation with the fault density exponent  $\gamma$  (Figure
- 393 7), and variation with the fluid resistivity ρ<sub>f</sub> (Figure 9). "Map-view" and "cross-section view"
- terms refer to Figure 1.

#### 4.2.1 Base case

395

- Reservoir-scale permeability is highest along-strike (1×10<sup>-12</sup> m<sup>2</sup>). Vertical reservoir-scale
- 397 permeability is intermediate in magnitude  $(4\times10^{-14} \text{ m}^2)$ . The across-strike permeability is
- about an order of magnitude higher for the "map-view" than the "cross-section view" models
- i.e.,  $9\times10^{-14}$  m<sup>2</sup> versus  $4\times10^{-15}$  m<sup>2</sup>, with the median (in log-space) equal to  $2\times10^{-14}$  i.e. slightly
- 400 lower than vertical permeability. The contribution of micro-faults to the overall permeability
- 401 is low in all cases ( $<2\times10^{-16}$  m<sup>2</sup>). Permeability anisotropy is  $\sim50$  (along/across-strike), and 2
- 402 (vertical/across-strike), however there is significant uncertainty around these numbers
- 403 (visualised by shaded ranges in Figure 6) due to uncertainty in the across-strike permeability.
- Along-strike and vertical resistivity are similar, 190 and 230  $\Omega$ m respectively, while across-
- strike resistivity is well-constrained (compared to permeability) at 465 ( $\pm$ 30)  $\Omega$ m.
- 406 Correspondingly, along-strike/vertical resistivity ratio is close to 1 (0.8) while along/across-
- strike and vertical/across-strike resistivity anisotropy ratios are around 0.38 and 0.47
- 408 respectively. Micro-scale resistivity anisotropy is almost the same as reservoir-scale, i.e. most
- of the inferred anisotropy is due to micro-scale faults.

#### 410 **4.2.2 Influence of P**<sub>z</sub>

- The proportion of along-strike faults, P<sub>z</sub>, has a moderate impact on permeability in the range
- 412 0.7 to 0.9, with along-strike and vertical permeability decreasing by a factor of five over this
- 413 range. Across-strike permeability decreases by slightly more over this range, so anisotropy
- ratio increases. Between  $P_z = 0.9$  and 1.0, along-strike and vertical permeability drops nearly
- 415 to micro-fault level ( $<1\times10^{-15}$ ), and across-strike permeability drops to matrix values.
- Therefore, at least 10% of cross-faults are needed to provide a fully connected network.
- There is a peak in permeability anisotropy ratio at about P<sub>z</sub>=0.95, beyond which the lack of
- 418 connectivity of the fault network causes low permeabilities in all directions.

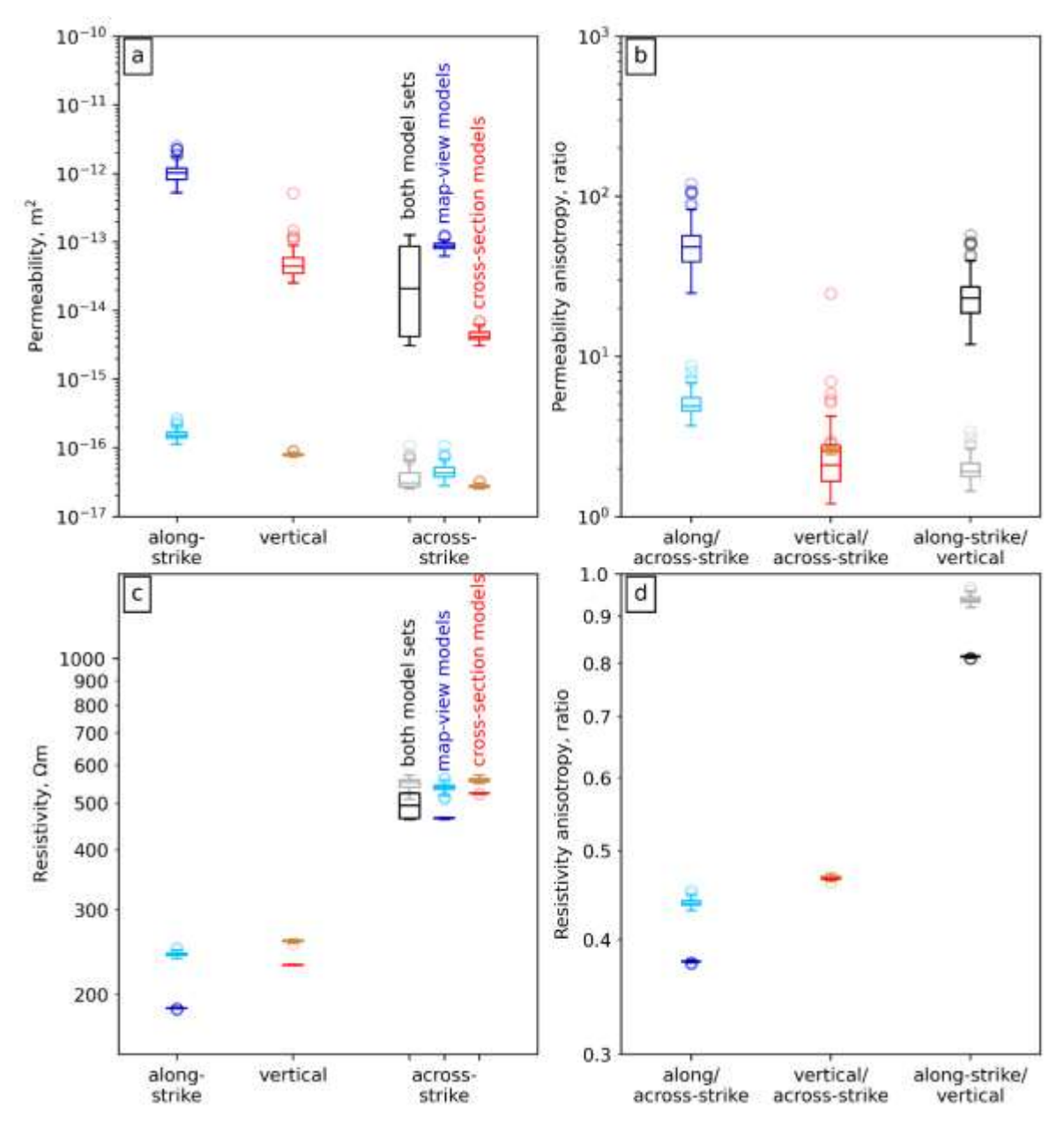


Figure 5. Permeability and resistivity of a faulted reservoir from modelling shown as box and whisker plots. (a) along-strike, vertical, and across-strike permeability in a normal faulting (TVZ-type) regime, with across-strike given as both individual plots for the map-view and cross-section view models, as well as a single box and whisker for all across-strike models combined, (b) along/across-strike, vertical/across-strike, and along-strike/vertical permeability anisotropy ratios, using the median across both across-strike models. (c) and (d) show equivalents to (a) and (b) for resistivity. Light coloured boxes represent 'micro-fault' permeability determined by modelling an  $0.5 \times 0.5$  m area containing faults  $\leq 0.2$  m in size. Darker boxes represent 'macro-scale' permeability determined by modelling a  $80 \times 80$  m area. Boxes show the  $25^{th}$  and  $75^{th}$  percentile with line at the median (computed in log space), fliers are shown semi-transparent to aid visualisation of clusters of points.

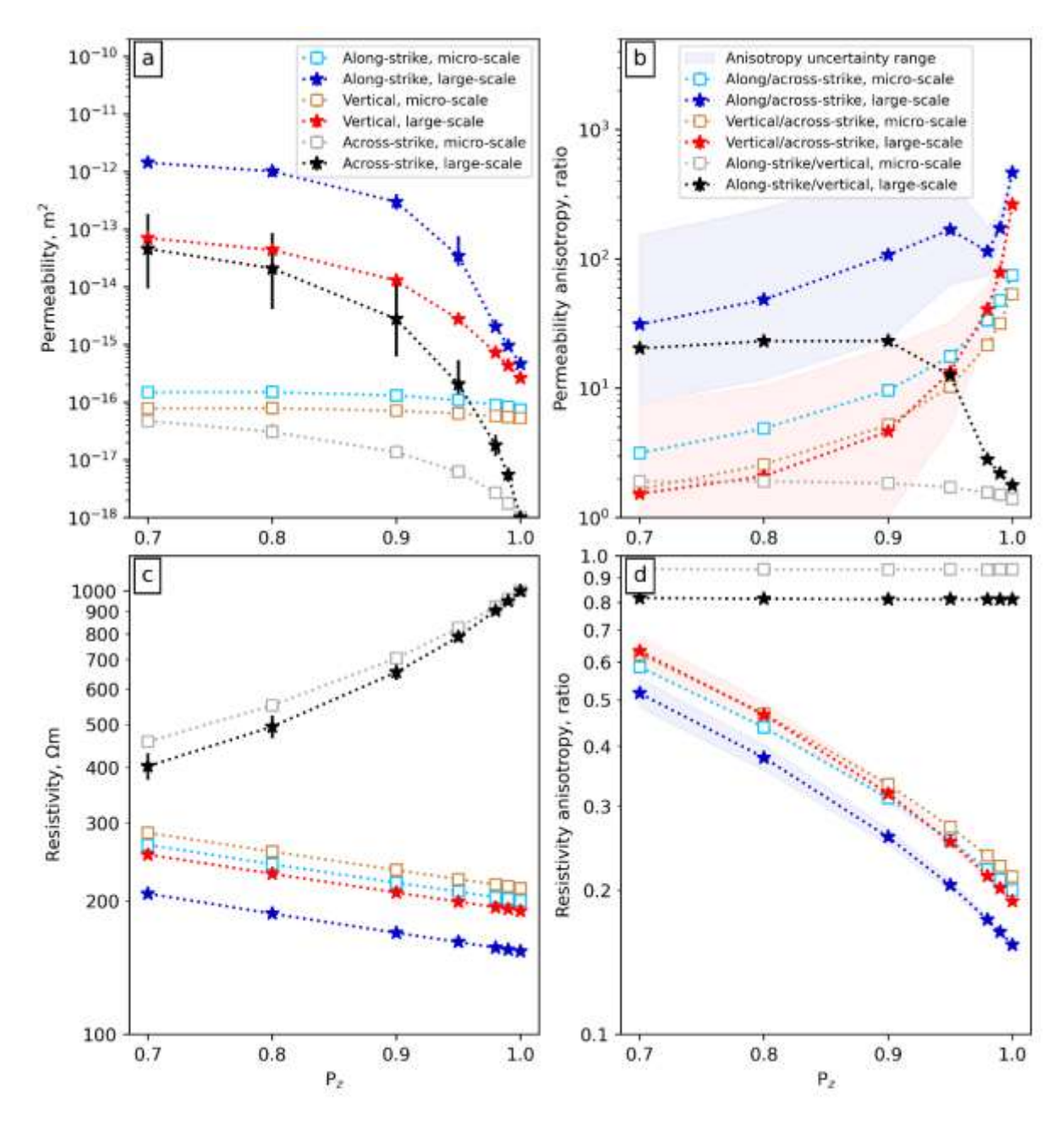


Figure 6. Permeability and resistivity as a function of the proportion of faults along the dominant strike direction (Pz). (a) permeability in three directions (b) corresponding permeability anisotropy ratios, (c) resistivity in three directions, and (d) corresponding resistivity anisotropy ratios. (a) and (c) are shown as error bar plots with the errorbars representing the inter-quartile range, (b) and (d) are shown as points with error ranges shaded in the along-strike and vertical cases representing the range due to using either of the two different across-strike results to compute the anisotropy ratio as opposed to the median of both (symbols and dotted lines).

 Along/across-strike resistivity anisotropy ratio decreases with  $P_z$ , to a minimum of 0.16 for  $P_z$ =1.0. This contrasts with permeability anisotropy which is highest at  $P_z$ =0.95 and very low for higher  $P_z$ . The increase in anisotropy ratio is mainly due to an increase in across-strike resistivity, as the along-strike resistivity only decreases by 25 % over the tested  $P_z$  range (Figure 6).

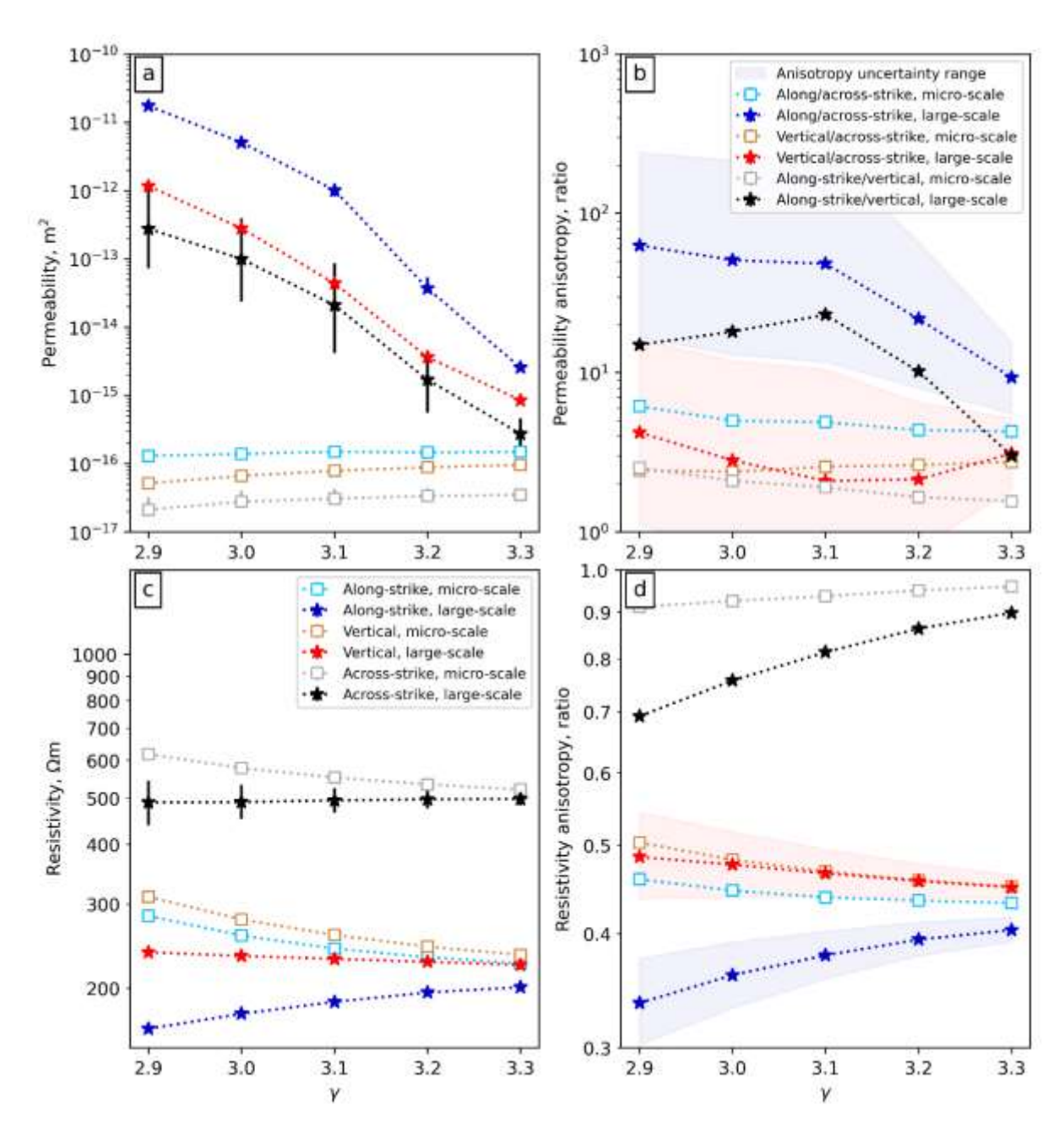


Figure 7. Permeability and resistivity as a function of the fault density exponent  $\gamma$ . (a) permeability in three directions (b) corresponding permeability anisotropy ratios, (c) resistivity in three directions, and (d) corresponding resistivity anisotropy ratios. (a) and (c) are shown as error bar plots with the errorbars representing the inter-quartile range, (b) and (d) are shown as points with error ranges shaded in the along-strike and vertical cases representing the range due to using either of the two different across-strike results to compute the anisotropy ratio as opposed to the median of both (symbols and dotted lines).

#### 4.2.3 Influence of fault density exponent

The value of the exponent  $\gamma$ , which controls the relative numbers of long vs short faults, strongly controls reservoir-scale permeability, but has only a small impact on micro-fracture permeability (Figure 7). An increase of  $\gamma$  from 2.9 to 3.3 (i.e., progressively reducing the relative number of long faults) decreases reservoir-scale permeability by about four orders of magnitude. On the other hand, micro-scale permeability barely changes over this range. This suggests that the large faults have a greater effect on permeability than the more numerous smaller faults.

In contrast,  $\gamma$  has a minor influence on resistivity and resistivity anisotropy. Along-strike resistivity increases by 22 % over the tested range, while both vertical and along-strike resistivity change by <7 %. Accordingly, there is a small change in along/across-strike resistivity ratio over this  $\gamma$  range (0.33 to 0.4).

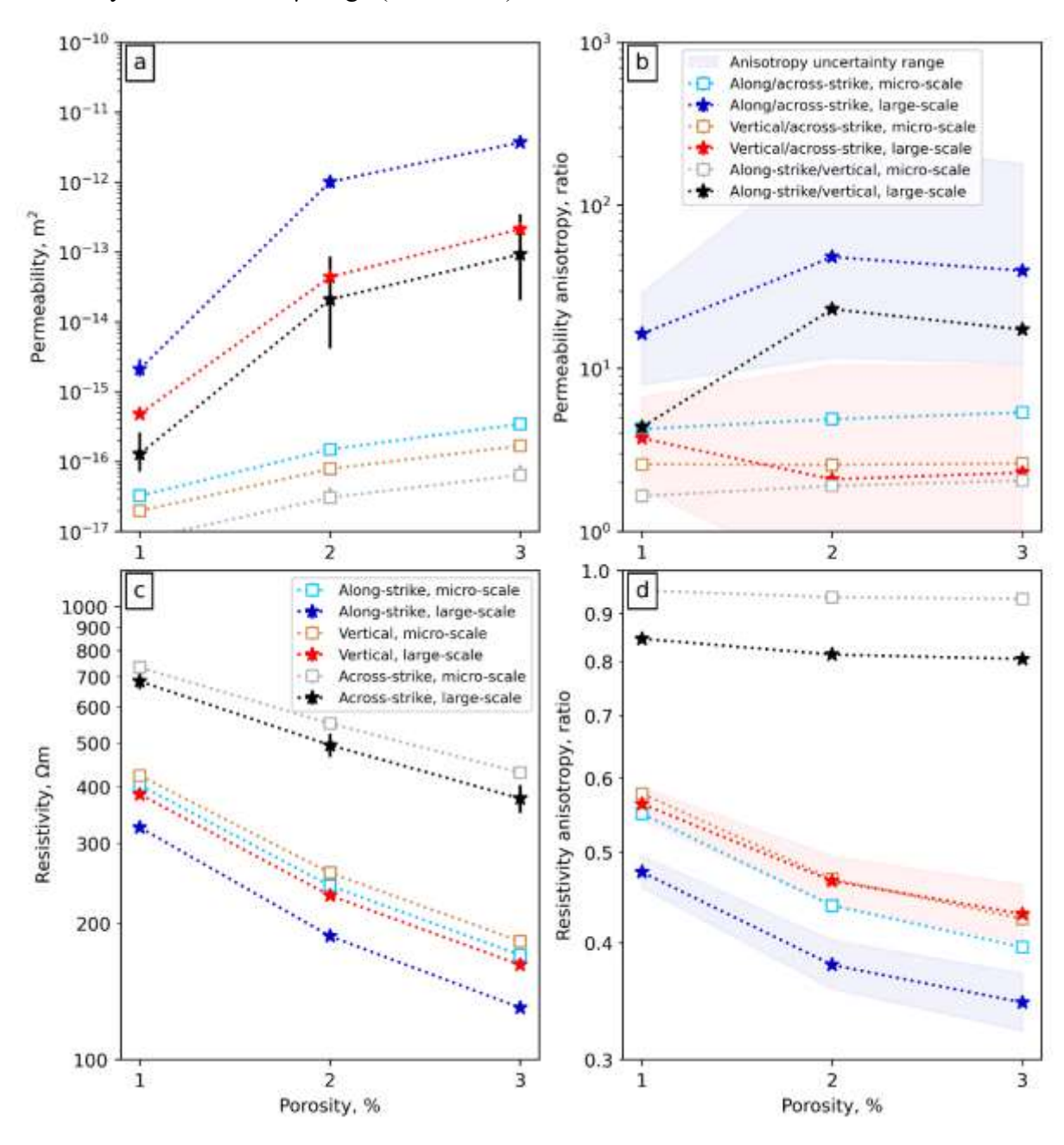


Figure 8. Permeability and resistivity as a function of fracture porosity. (a) permeability in three directions (b) corresponding permeability anisotropy ratios, (c) resistivity in three directions, and (d) corresponding resistivity anisotropy ratios. (a) and (c) are shown as error bar plots with the errorbars representing the inter-quartile range, (b) and (d) are shown as points with error ranges shaded in the along-strike and vertical cases representing the range due to using either of the two different across-strike results to compute the anisotropy ratio as opposed to the median of both (symbols and dotted lines).

#### 4.2.4 Influence of porosity

Both micro-fracture and reservoir-scale permeability increases with fracture porosity as may be expected, however this is non-linear, likely because the 1%-porosity fault volumes are

below their fluid-flow percolation threshold. A porosity increase from 1 to 2 % results in

permeability increasing by two orders of magnitude, while an increase from 2 to 3 %

increases permeability by a factor of 3-5 (Figure 8).

Porosity is the strongest control on resistivity, with a change from 1 to 3 % decreasing alongstrike resistivity by a factor of 2.5. Along/across-strike resistivity ratio changes from 0.48 to

476 0.35 over this porosity range.

#### 4.2.5 Influence of fluid resistivity

Median bulk resistivity anisotropy follows a near-sigmoidal relationship as a function of the ratio of matrix to fluid resistivity  $\rho_m/\rho_f$  (in log-log space), increasing again at very low fluid resistivities (Figure 9). This means that very low fluid resistivities by themselves don't increase the anisotropy ratio of a reservoir much beyond a factor of around 3. However, a combination of very low proportion of faults across the dominant strike, with low fluid resistivities, may increase the anisotropy ratio higher than in the presented models.

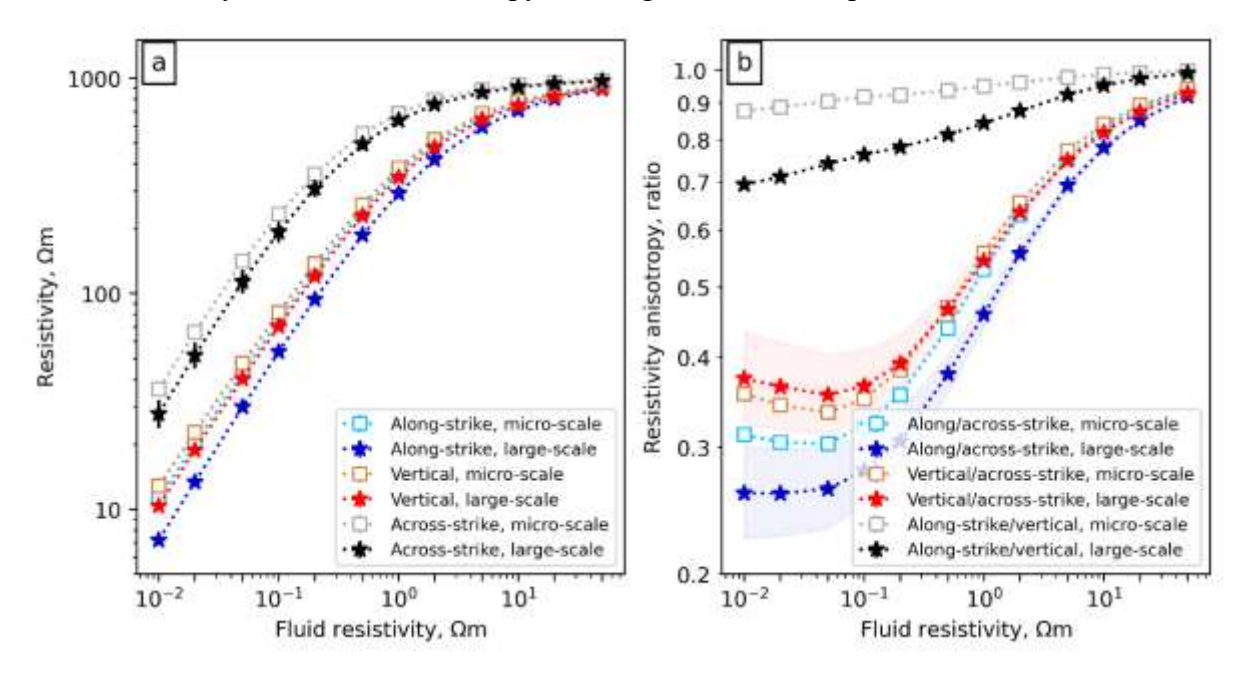


Figure 9. Resistivity as a function of fluid resistivity. (a) resistivity in three directions, and (b) corresponding resistivity anisotropy ratios. (a) shown as error bar plots with the errorbars representing the inter-quartile range, (b) is shown as points with error ranges shaded in the along-strike and vertical cases representing the range due to using either of the two different across-strike results to compute the anisotropy ratio as opposed to the median of both (symbols and dotted lines).

#### 5. Discussion

#### 5.1 Comparison to field measurements and other models

Field measurements and models developed with other approaches provide a means to assess the validity of the numerical model results. For permeability, reservoir models calibrated to reservoir pressure and temperature histories provide a ground-truth. For resistivity, ground-truthing data includes borehole resistivity logs and geophysical data.

#### 5.1.1 Permeability

- Bulk vertical permeability in geothermal reservoir models ranges from around 10<sup>-15</sup> to 10<sup>-13</sup>
- 499 m<sup>2</sup> in TVZ fields (Dempsey et al. 2011, Baars et al. 2023, van Driel et al. 2023, Rajput et al.
- 500 2024). Permeability is unlikely to be much higher than this on a large scale as it is difficult to
- retain stable convection (Scott et al. 2016, Pearson-Grant and Bertrand 2021). Fault models
- presented here have vertical and across-strike permeabilities consistent with those of isotropic
- 503 permeability in reservoir models (Figure 5a).
- 504 Discrete fracture network-derived permeability model based on a TVZ-like setting presented
- by (Kissling and Massiot 2023) used a different approach and offers a useful comparison.
- Those models were 2D, in "cross-section" view. Fractures were modelled as sticks with a
- 507 constant length to aperture ratio but had a range of fracture dip magnitudes rather than
- 508 constraining fault orientation to two orthogonal directions. The β factor, which relates
- geometric to hydraulic aperture, is different in Kissling and Massiot (2023) ( $\beta$ =0.002) to our
- models ( $\beta$ =0.185), but this is because their geometric aperture represents the total width of
- the fracture, different from our mean aperture. Additionally, we find that the fault length-
- aperture relationship is a power law with exponent <1 (Equation 6), i.e., larger fractures have
- smaller apertures relative to length than smaller fractures. Consequently, their models have
- less permeable faults than us, but with higher fracture porosity. Overall, modelled reservoir-
- scale vertical permeabilities of Kissling and Massiot (2023) are very similar to our models
- $(3\times10^{-14} \text{ to } 1.3\times10^{-13} \text{ m}^2)$ , vs  $4\times10^{-14} \text{ in this paper}$ . If we consider the across-strike result from
- our "cross-section" models (Figure 5), then the across-strike permeabilities and
- 518 horizontal/vertical permeability anisotropy ratio (~13) are also very similar to our models.
- 519 Conversely, permeability of individual faults measured in the lab (Watanabe et al. 2008,
- Watanabe et al. 2009, Ishibashi et al. 2015) generally report permeabilities higher than from
- our models, e.g. for faults with no displacement, measured permeabilities are around 10<sup>-12</sup> to
- 522  $10^{-11}$  m<sup>2</sup>, compared to  $10^{-13}$  to  $10^{-12}$  m<sup>2</sup> in our models. For faults with 5 mm displacement,
- measured permeabilities of 10<sup>-9</sup> to 10<sup>-8</sup> m<sup>2</sup> are about an order of magnitude higher than our
- models. However, this difference can be explained by the fact that induced faults generally
- have higher roughness amplitude (scaling factor) than natural faults (Figure 3) and scaling
- factor has a strong effect on permeability. For example, halving scaling factor reduces
- 527 permeability by an order of magnitude (Sawayama et al. 2023).

#### 5.1.2 Resistivity

528

- In geothermal wells, downhole resistivity measurements are rarer than surface geophysical
- techniques and only penetrate up to  $\sim 1$  m into the formation. However, they provide greater
- certainty on absolute resistivity. At the Ngā Tamariki geothermal field, New Zealand,
- reservoir resistivity was measured at  $30 100 \Omega m$ , lower than our models. This may reflect a
- lower host rock resistivity which was primarily tuff and volcaniclastic rocks.
- The primary surface geophysical technique used to measure resistivity in geothermal
- reservoirs is MT as it is normally the only method with enough depth penetration to image
- reservoirs at >2km depth. Absolute resistivity variations from MT inversion are sensitive to
- 538 the prior model (Robertson et al. 2020), compounded by reduced sensitivity below the
- conductive clay cap in geothermal systems. However, resistivities of 100 to 200  $\Omega$ m, which
- we predict for reservoirs containing 0.5  $\Omega$ m fluid and 1000  $\Omega$ m rock matrix, are consistent

- with resistivity in the reservoir zone in MT inversions of TVZ geothermal systems (e.g.,
- Heise et al. 2008, Bertrand et al. 2013, Heise et al. 2016, Bertrand et al. 2022).
- There are few conclusive measurements of resistivity anisotropy measured from the surface,
- and there is likely high uncertainty in anisotropy ratios due to the ambiguity between
- anisotropy and 2D/3D structure. An experiment designed to measure resistivity anisotropy
- using controlled-source electromagnetic (EM) data over the East Pacific Rise found
- resistivity along-strike of the mid ocean ridge approximately 18-36 times lower than
- 548 perpendicular to it, interpreted as sub-vertical fault zones (Chesley et al. 2019). These ratios
- are higher than determined from our models. Being in saltwater, fluid resistivities beneath the
- East Pacific Rise may be lower than our modelled fluid resistivities and this combined with a
- higher proportion of along-strike faults may produce anisotropy ratios encompassing the
- measured range. Alternatively the inconsistency may reflect uncertainty in the EM inversions;
- 553 geophysical inversions are non-unique, and EM inversions can overestimate extreme values;
- the 70 and 90<sup>th</sup> percentile scenarios reported by Chesley et al. (2019) encompassed scenarios
- with anisotropy ratios as low as a factor of about 3, consistent with our results (Figure 9).
- 556 At the other end of the fluid resistivity scale, resistivity anisotropy was measured using the
- 557 DC resistivity method for understanding fractured aquifers (Lane Jr et al. 1995, Odoh and
- Onwuemesi 2009, George et al. 2010, Yeboah-Forson and Whitman 2014, Ani et al. 2023).
- Water resistivity is only reported in one of these studies (14  $\Omega$ m), however we assume that
- groundwater intended as drinking/irrigation supply is likely to have a relatively high
- resistivity,  $>10 \Omega$ m based on an assumption of <250 ppm NaCl from World Health
- Organization guidelines (World Health Organisation 2023) and <30°C (Light et al. 2005).
- Reported anisotropy ratios in these studies of around 1.01 to 1.4 are consistent with our
- models for fluid resistivity  $> 10 \Omega \text{m}$ .

#### 5.2 Implications for geothermal exploration

- Modelling predicts that the fault permeability perpendicular to slip is about seven times
- higher than that parallel. In an extensional regime like the TVZ, this would mean that vertical
- 568 permeability is lower than horizontal along-strike permeability. This result numerically
- demonstrates the qualitative prediction that fault irregularities should enhance permeability
- most strongly along the direction perpendicular to slip (Sibson 2000, Rowland and Simmons
- 571 2012). Analogous to permeability, fault resistivity perpendicular to fault slip is lower than
- that parallel to slip, though by about a smaller factor of 2-3 (Figure 4). In reservoir models,
- 573 the highest pressure gradients are likely vertical due to the competition between buoyancy
- and gravitational forces. It would be useful to test the sensitivity of these reservoir models to
- along-strike permeability. If there is only a weak pressure gradient along-strike, then there
- may be little sensitivity in the models to along-strike permeability.
- In general, resistivity shows much lower sensitivity to fault length distribution and porosity
- 578 than permeability. Therefore, there are many permeability scenarios consistent with a given
- resistivity. Consequently, resistivity-based techniques alone are unlikely to be able to
- uniquely map permeability. However, there are some aspects of the resistivity tensor that may
- be useful in understanding permeability distribution within a reservoir and particularly
- 582 directional dependence of permeability.
- Since across-strike resistivity is uniformly higher than along-strike resistivity, then if the host
- rock is isotropic and fractures are fluid filled, measuring the resistivity tensor should resolve

- 585 the orientation of the most permeable structures. In MT, and other surface-based resistivity
- surveying techniques, resistivities of 190  $\Omega$ m (along-strike) and 470  $\Omega$ m (across-strike) may
- be resolvable near the surface, as shown in groundwater studies (Section 5.1.2). However,
- beneath a conductive clay surface layer with resistivity  $\sim 3 \Omega m$  these resistivities are likely to
- be a subtle signal, difficult to uniquely resolve. A potential avenue of future work could be to
- examine the potential for utilising borehole to borehole measurements to measure resistivity
- 591 within a reservoir, including the possibility of using steel boreholes as long electrodes
- (Rucker et al. 2011, Zhang et al. 2014, Heagy and Oldenburg 2019), which would avoid
- signal needing to penetrate a conductive surface layer. Additionally, well logging tools to
- determine directional resistivity are applied in the petroleum industry (Leveridge 2010,
- Horstmann et al. 2015, Wang et al. 2020). If such tools could be developed to handle
- 596 geothermal conditions, they may be a useful tool for understanding geothermal reservoir
- 597 permeability.

- Along-strike, vertical and across strike resistivity are nearly equally sensitive to porosity, so
- resistivity anisotropy ratio is not highly sensitive to porosity. Since resistivity is also sensitive
- to matrix resistivity (controlled by lithology, alteration, temperature etc), it would be
- necessary to accurately characterise matrix resistivity (e.g. using core measurements) before
- absolute resistivity could be used as a proxy for porosity.
- Across-strike resistivity (and consequently, resistivity anisotropy) is most sensitive to the
- proportion of along-strike faults, or P<sub>z</sub>. If we assume that matrix resistivity is isotropic, then
- resistivity anisotropy may be useful in mapping relative proportions of faults along different
- directions, and thus targeting permeable zones within a reservoir.

#### 5.3 Model limitations and next steps

- This work represents an important next step in linking electrical resistivity and permeability
- at the core to field scale. However, the approach has several limitations that could be
- addressed in future work.
- Firstly, the models are 2D, so full resistivity and permeability tensors are not captured.
- 612 Implementing the approach in 3D would capture the effects of interactions between
- differently oriented faults in three directions, and fault intersections. Secondly, the modelling
- 614 is carried out on orthogonal axes, rather than using the true geometry of faults, which show a
- range of orientations. Allowing arbitrary orientations would make the models more realistic.
- Thirdly, the cells are 80 x 80 m, which is similar in scale to a single cell in reservoir models
- 617 (Baars et al. 2023, O'Sullivan et al. 2025). Upscaling the models further requires careful
- consideration of damage zones and gouge in faults. These are likely to result in permeabilities
- 619 that are lower than what we have modelled due to reduced aperture sizes compared to a single
- fault with no damage, unless compensated by increased density of secondary faults in the
- damage zone (Faulkner et al. 2010).
- The fractures are assumed to contain only fluids, and of course, if some of the fractures are
- mineralised or filled with clay, they may be conductive but not permeable and have effects on
- resistivity that are not expressed in permeability. These effects, which also hinder borehole
- image interpretation, could be understood further through measurements on core and outcrop
- to identify the characteristics, and extent of conductive but not permeable zones. Joint

- 627 inversion of seismic anisotropy and resistivity may have the potential to remove some of this
- ambiguity and help to image permeable fracture zones.
- Finally, both fluid and current are modelled using simplified models, although these are likely
- 630 to be adequate given other uncertainties in the modelling. Permeability and resistivity are
- modelled using, respectively, the modified local parallel plate model, and Ohm's Law,
- excluding any surface conductance or frequency dependent effects. The local parallel plate
- model is likely to be a reasonable approximation given the high sensitivity of the
- permeability calculations to inputs, i.e. changes in porosity,  $\gamma$  and  $P_z$  result in orders of
- magnitude changes in permeability. Thus errors due to mis-characterisation of model inputs
- are likely to dominate over inaccuracies in the parallel plate model which are estimated to be
- 637 <10 % for low flow rates (Brush and Thomson 2003). Neglecting surface conductance and
- frequency-dependent conductivity are likely to have minimal effect on the overall
- conductivity, with data suggesting small effects relative to the bulk electrolyte conductivity,
- with a smaller relative effect at high salinities and temperatures (Revil and Glover 1998).
- However, surface conductivity effects in very high temperatures (e.g. supercritical) are
- unknown and could potentially be significant.

#### 6. Conclusions

643

662

664

- Two-dimensional numerical modelling of a faulted reservoir has estimated, for the first time,
- direction-dependent permeability and resistivity at reservoir scale (80 x 80 m), linking
- resistivity with permeability, and linking the core to the reservoir scale. Permeability is
- highest in the horizontal along-dominant-strike direction, lower vertically, and lowest in the
- 648 horizontal across-dominant strike direction. Resistivity is lowest along the dominant strike,
- slightly higher in the vertical direction and highest across-strike. While these differences in
- resistivity with orientation are likely detectable if present at the surface, it may be challenging
- to resolve these beneath a conductive clay cap of a geothermal field.
- Resistivity has low sensitivity to fracture length distribution, with all resistivity predictions
- 653 for a given direction within a factor of 2-3. Resistivity shows highest sensitivity to fracture
- porosity and the proportion of along-strike faults. Permeability shows strong sensitivity to
- fracture length distribution and porosity. There is a range of about four orders of magnitude
- across the different parameter combinations.
- Resistivity anisotropy is one of the least sensitive parameters to model inputs, remaining
- relatively constant for different fault network parameters. It shows strongest sensitivity to the
- proportion of faults along the dominant strike direction (Pz). Conversely, permeability along
- the dominant strike of the fault zone is not highly sensitive to P<sub>z</sub>, except at very high P<sub>z</sub>
- values where the lack of across-strike faults inhibits a full fault network connection.

#### 7. Data statement

The code used for these models is available at https://github.com/alkirkby/resistor\_network.

#### 8. Acknowledgements

- The authors would like to thank Warwick Kissling for useful discussions and for reviewing
- an earlier version of this paper. This project was supported by the New Zealand Ministry of
- Business, Innovation and Employment (MBIE) through the Energy Futures programme
- 668 (Strategic Science Investment Fund, contract C05X1702).

- 669 9. References
- Ani, C. C., C. Akpa, P. N. Obasi and A. Chukwu (2023). "Integrated electrical resistivity methods for
- evaluation of fracture terrain groundwater potentials, case study of indurated shale of Lower Benue
- trough, Southeastern Nigeria." <u>Groundwater for Sustainable Development</u> 23: 101014.
- Ardid, A., D. Dempsey, E. Bertrand, F. Sepulveda, P. Tarits, F. Solon and R. Archer (2021). "Bayesian
- magnetotelluric inversion using methylene blue structural priors for imaging shallow conductors in
- geothermal fields." Geophysics **86**(3): E171-E183.
- Baars, M., T. Renaud, J. Riffault, M. J. O'Sullivan, J. O'Sullivan, M. Gravatt, K. Dekkers and M.
- 677 Speetjens (2023). Numerical model of the Tikitere geothermal system. 45th New Zealand Geothermal
- 678 Workshop. Auckland, New Zealand.
- Bahr, K. (1997). "Electrical anisotropy and conductivity distribution functions of fractal random
- networks and of the crust: the scale effect of connectivity." Geophysical Journal International 130(3):
- 681 649-660.
- Bannard, J. E. (1975). "Effect of density on the electrical conductance of aqueous sodium chloride
- solutions." Journal of Applied Electrochemistry 5(1): 43-53.
- Bertrand, E. A., T. G. Caldwell, S. Bannister, S. Soengkono, S. L. Bennie, G. J. Hill and W. Heise
- 685 (2015). "Using array MT data to image the crustal resistivity structure of the southeastern Taupo
- 686 Volcanic Zone, New Zealand." Journal of Volcanology and Geothermal Research 305: 63-75.
- Bertrand, E. A., T. G. Caldwell, G. J. Hill, S. L. Bennie and S. Soengkono (2013). "Magnetotelluric
- imaging of the Ohaaki geothermal system, New Zealand: Implications for locating basement
- permeability." <u>Journal of Volcanology and Geothermal Research</u> **268**: 36-45.
- 690 Bertrand, E. A., P. Kannberg, T. G. Caldwell, W. Heise, S. Constable, B. Scott, S. Bannister, G.
- Kilgour, S. L. Bennie, R. Hart and N. Palmer (2022). "Inferring the magmatic roots of volcano-
- 692 geothermal systems in the Rotorua Caldera and Okataina Volcanic Centre from magnetotelluric
- models." <u>Journal of Volcanology and Geothermal Research</u> **431**: 107645.
- 694 Bibby, H. M., T. G. Caldwell, F. J. Davey and T. H. Webb (1995). "Geophysical evidence on the
- 695 structure of the Taupo Volcanic Zone and its hydrothermal circulation." Journal of Volcanology and
- 696 Geothermal Research **68**(1): 29-58.
- Bolós, X., G. Cifuentes, J. L. Macías, G. Sosa-Ceballos, F. Garcia-Tenorio and M. Albor (2019).
- "Geophysical imaging of fluid circulation and its relation with the structural system of Cerritos
- 699 Colorados geothermal field, La Primavera caldera (Mexico)." <u>Journal of Volcanology and Geothermal</u>
- 700 Research **369**: 238-249.
- Bonnet, E., O. Bour, N. E. Odling, P. Davy, I. Main, P. Cowie and B. Berkowitz (2001). "Scaling of
- fracture systems in geological media." <u>Reviews of Geophysics</u> **39**(3): 347-383.
- Brown, S. R. (1989). "Transport of fluid and electric current through a single fracture." <u>Journal of</u>
- Geophysical Research: Solid Earth **94**(B7): 9429-9438.
- Brown, S. R. (1995). "Simple mathematical model of a rough fracture." Journal of Geophysical
- 706 Research: Solid Earth **100**(B4): 5941-5952.
- Brown, S. R. and C. H. Scholz (1986). "closure of rock joints." <u>Journal of Geophysical Research:</u>
- 708 Solid Earth **91**(B5): 4939-4948.
- Browne, P. R. L. (1970). "Hydrothermal alteration as an aid in investigating geothermal fields."
- 710 <u>Geothermics</u> **2**: 564-570.
- Brush, D. J. and N. R. Thomson (2003). "Fluid flow in synthetic rough-walled fractures: Navier-
- 712 Stokes, Stokes, and local cubic law simulations." Water Resources Research 39(4).
- 713 Calibugan, A., K. Melia and M. Rivera (2022). Conceptual model update for the Rotokawa
- geothermal field, New Zealand. 44th New Zealand Geothermal Workshop. Auckland, New Zealand:
- 715 8.

- 716 Candela, T., F. Renard, Y. Klinger, K. Mair, J. Schmittbuhl and E. E. Brodsky (2012). "Roughness of
- fault surfaces over nine decades of length scales." <u>Journal of Geophysical Research: Solid Earth</u>
- 718 **117**(B8).
- 719 Cant, J. L., P. A. Siratovich, J. W. Cole, M. C. Villeneuve and B. M. Kennedy (2018). "Matrix
- 720 permeability of reservoir rocks, Ngatamariki geothermal field, Taupo Volcanic Zone, New Zealand."
- 721 Geothermal Energy **6**(1): 2.
- 722 Chambefort, I., E. Buscarlet, I. C. Wallis, S. Sewell and M. Wilmarth (2016). "Ngatamariki
- Geothermal Field, New Zealand: Geology, geophysics, chemistry and conceptual model."
- 724 <u>Geothermics</u> **59**: 266-280.
- Chambefort, I., B. Lewis, C. J. N. Wilson, A. J. Rae, C. Coutts, G. Bignall and T. R. Ireland (2014).
- 726 "Stratigraphy and structure of the Ngatamariki geothermal system from new zircon U–Pb
- geochronology: Implications for Taupo Volcanic Zone evolution." <u>Journal of Volcanology and</u>
- 728 Geothermal Research **274**: 51-70.
- 729 Chen, G. and H. Spetzler (1993). "Topographic characteristics of laboratory induced shear fractures."
- 730 pure and applied geophysics **140**(1): 123-135.
- 731 Chesley, C., K. Key, S. Constable, J. Behrens and L. MacGregor (2019). "Crustal Cracks and Frozen
- Flow in Oceanic Lithosphere Inferred From Electrical Anisotropy." Geochemistry, Geophysics,
- 733 <u>Geosystems</u> **20**(12): 5979-5999.
- Dempsey, D., J. V. Rowland, R. Archer and S. Ellis (2011). Modelling geothermal circulation in a
- 735 "TVZ-like" setting. New Zealand Geothermal Workshop. Auckland, New Zealand.
- Dezayes, C., G. Albert and V. Benoît (2010). "Structure of the low permeable naturally fractured
- 737 geothermal reservoir at Soultz." <u>Comptes Rendus. Géoscience</u> **342**(7-8): 517-530.
- 738 Fathi, A., Z. Moradian, P. Rivard, G. Ballivy and A. J. Boyd (2016). "Geometric Effect of Asperities
- on Shear Mechanism of Rock Joints." Rock Mechanics and Rock Engineering 49(3): 801-820.
- Faulkner, D. R., C. A. L. Jackson, R. J. Lunn, R. W. Schlische, Z. K. Shipton, C. A. J. Wibberley and
- 741 M. O. Withjack (2010). "A review of recent developments concerning the structure, mechanics and
- fluid flow properties of fault zones." Journal of Structural Geology **32**(11): 1557-1575.
- Franzson, H., R. Zierenberg and P. Schiffman (2008). "Chemical transport in geothermal systems in
- 744 Iceland: Evidence from hydrothermal alteration." <u>Journal of Volcanology and Geothermal Research</u>
- 745 **173**(3): 217-229.
- George, A. M., A. A. Okiwelu and D. A. Obi (2010). "DC-resistivity estimation of second porosity
- and anisotropy using azimuthal resistivity surveys: A case study of part of Oban Massif and Obudu
- Plateau, southeastern, Nigeria." Research Journal of Earth Sciences 2(2): 24-29.
- Heagy, L. J. and D. W. Oldenburg (2019). "Modeling electromagnetics on cylindrical meshes with
- applications to steel-cased wells." <u>Computers & Geosciences</u> **125**: 115-130.
- Heap, M. J. and B. M. Kennedy (2016). "Exploring the scale-dependent permeability of fractured
- andesite." Earth and Planetary Science Letters 447: 139-150.
- Hedenquist, J. W. (1983). <u>Characteristics of Broadlands Ohaaki water chemistry, and changes</u>
- subsequent to initial production. Proceedings of the New Zealand Geothermal Workshop.
- Hedenquist, J. W. (1990). "The thermal and geochemical structure of the broadlands-ohaaki
- 756 geothermal system, new zealand." Geothermics 19(2): 151-185.
- Heise, W., T. G. Caldwell, E. A. Bertrand, G. J. Hill, S. L. Bennie and N. G. Palmer (2016). "Imaging
- 758 the deep source of the Rotorua and Waimangu geothermal fields, Taupo Volcanic Zone, New
- 759 Zealand." <u>Journal of Volcanology and Geothermal Research</u> **314**: 39-48.
- Heise, W., T. G. Caldwell, H. M. Bibby and S. C. Bannister (2008). "Three-dimensional modelling of
- 761 magnetotelluric data from the Rotokawa geothermal field, Taupo Volcanic Zone, New Zealand."
- Geophysical Journal International **173**(2): 740-750.

- Horstmann, M., K. Sun, P. Berger, P. A. Olsen, D. Omeragic, S. Crary, R. Griffiths and A. Abubakar
- 764 (2015). Resistivity Anisotropy and Formation Dip Evaluation in Vertical and Low Angle Wells using
- 765 LWD Directional Electromagnetic Measurements. SPWLA 56th Annual Logging Symposium:
- 766 SPWLA-2015-LLLL.
- Hou, J., B. Donderici and D. Torres (2016). "Enhanced real-time determination of resistivity
- anisotropy and dip using multifrequency and multicomponent induction logging." <u>Interpretation</u> 4(2):
- 769 SF137-SF149.
- 770 Ikhwan, M., I. C. Wallis and J. V. Rowland (2020). Geological Model and Permeability Framework of
- 771 <u>Bukit Daun Geothermal Field, Indonesia</u>. New Zealand Geothermal Workshop, Waitangi, New
- 772 Zealand.
- 1773 Intani, R. G., G. U. Golla, Y. Syaffitri, H. M. Paramitasari, G. A. Nordquist, C. Nelson, Ginanjar, G.
- 774 K. D. S. Giri and A. Sugandhi (2020). "Improving the conceptual understanding of the Darajat
- 775 Geothermal Field." Geothermics 83: 101716.
- Ishibashi, T., N. Watanabe, N. Hirano, A. Okamoto and N. Tsuchiya (2015). "Beyond-laboratory-scale
- prediction for channeling flows through subsurface rock fractures with heterogeneous aperture
- distributions revealed by laboratory evaluation." <u>Journal of Geophysical Research: Solid Earth</u> **120**(1):
- 779 106-124.
- 780 Ishizu, K., Y. Ogawa, K. Nunohara, N. Tsuchiya, M. Ichiki, H. Hase, W. Kanda, S. Sakanaka, Y.
- Honkura, Y. Hino, K. Seki, K. H. Tseng, Y. Yamaya and T. Mogi (2022). "Estimation of Spatial
- 782 Distribution and Fluid Fraction of a Potential Supercritical Geothermal Reservoir by Magnetotelluric
- 783 Data: A Case Study From Yuzawa Geothermal Field, NE Japan." <u>Journal of Geophysical Research:</u>
- 784 <u>Solid Earth</u> **127**(2): e2021JB022911.
- Jolie, E., S. Scott, J. Faulds, I. Chambefort, G. Axelsson, L. C. Gutiérrez-Negrín, S. Regenspurg, M.
- 786 Ziegler, B. Ayling, A. Richter and M. T. Zemedkun (2021). "Geological controls on geothermal
- 787 resources for power generation." <u>Nature Reviews Earth & Environment</u> **2**(5): 324-339.
- Jylhänkangas, S. (2024). Comparing theoretical with measured seismic anisotropy in the Central
- 789 <u>Taupō Volcanic Zone</u>. MSc, Victoria University of Wellington.
- Kaya, E., M. J. O'Sullivan and A. Yeh (2014). "Three-dimensional model of the deep geothermal
- 791 resources in the Taupo-Reporoa Basin, New Zealand." <u>Journal of Volcanology and Geothermal</u>
- 792 Research **284**: 46-60.
- Kim, Y.-S. and D. J. Sanderson (2005). "The relationship between displacement and length of faults: a
- 794 review." Earth-Science Reviews **68**(3): 317-334.
- Kirkby, A. and G. Heinson (2017). "Three-dimensional resistor network modeling of the resistivity
- and permeability of fractured rocks." Journal of Geophysical Research: Solid Earth 122(4): 2653-
- 797 2669.
- 798 Kirkby, A., G. Heinson and L. Krieger (2016). "Relating permeability and electrical resistivity in
- fractures using random resistor network models." <u>Journal of Geophysical Research: Solid Earth</u>
- 800 **121**(3): 1546-1564.
- Kissling, W. M. and C. Massiot (2023). "Modelling of flow through naturally fractured geothermal
- reservoirs, Taupō Volcanic Zone, New Zealand." Geothermal Energy 11(1): 20.
- 803 Lane Jr, J. W., F. P. Haeni and W. M. Watson (1995), "Use of a Square-Array Direct-Current
- Resistivity Method to Detect Fractures in Crystalline Bedrock in New Hampshire." Groundwater
- **33**(3): 476-485.
- Lee, B., M. Unsworth, K. Árnason and D. Cordell (2020). "Imaging the magmatic system beneath the
- Krafla geothermal field, Iceland: A new 3-D electrical resistivity model from inversion of
- magnetotelluric data." Geophysical Journal International **220**(1): 541-567.
- Leveridge, R. M. (2010). "New Resistivity-Logging Tool Helps Resolve Problems of Anisotropy,
- 810 Shoulder-Bed Effects." Journal of Petroleum Technology **62**(08): 20-22.

- Light, T. S., S. Licht, A. C. Bevilacqua and K. R. Morash (2005). "The Fundamental Conductivity and
- Resistivity of Water." <u>Electrochemical and Solid-State Letters</u> **8**(1): E16.
- Liotta, D., A. Brogi, S. Árnadóttir, K. Ágústsson and U. Thorsteinsdóttir (2021). "Field evidence of
- the interplay between rift and transform structures in the Krafla geothermal area, N-Iceland."
- 815 <u>Geothermics</u> **91**: 102039.
- Martí, A. (2014). "The Role of Electrical Anisotropy in Magnetotelluric Responses: From Modelling
- and Dimensionality Analysis to Inversion and Interpretation." Surveys in Geophysics **35**(1): 179-218.
- Massiot, C., M. S. D., J. Siru, M. Nick, M. Regine and I. and Chambefort (2025). "Multi-scale
- 819 controls on veining in New Zealand greywacke basement rocks: implications for geothermal fluid
- 820 circulation." New Zealand Journal of Geology and Geophysics: 1-22.
- Massiot, C., S. D. Milicich, F. Sepulveda, M. J. Sophy, M. J. F. Lawrence, A. G. Griffin, M. Rickman,
- L. B. Carson, M. Rosenberg and M. Simpson (2023). "Highlights of Borehole Imaging, Tauhara
- Geothermal Field Drilling, New Zealand." <u>Proceedings, 45th New Zealand Geothermal Workshop,</u>
- 824 <u>15-17 November, 2023</u>.
- Massiot, C., A. Nicol, D. D. McNamara and J. Townend (2017). "Evidence for tectonic, lithologic,
- and thermal controls on fracture system geometries in an andesitic high-temperature geothermal
- field." <u>Journal of Geophysical Research: Solid Earth</u> **122**(8): 6853-6874.
- Matsuki, K., Y. Chida, K. Sakaguchi and P. W. J. Glover (2006). "Size effect on aperture and
- permeability of a fracture as estimated in large synthetic fractures." International Journal of Rock
- Mechanics and Mining Sciences **43**(5): 726-755.
- MBIE (2025). From the Ground Up: A draft strategy to unlock New Zealand's geothermal potential
- New Zealand, Ministry of Business, Innovation and Employment.
- McNamara, D. D., C. Massiot, B. Lewis and I. C. Wallis (2015). "Heterogeneity of structure and
- stress in the Rotokawa Geothermal Field, New Zealand." Journal of Geophysical Research: Solid
- 835 <u>Earth</u> **120**(2): 1243-1262.
- McNamara, D. D., S. D. Milicich, C. Massiot, P. Villamor, K. McLean, F. Sépulveda and W. F. Ries
- 837 (2019). "Tectonic Controls on Taupo Volcanic Zone Geothermal Expression: Insights From Te Mihi,
- Wairakei Geothermal Field." Tectonics **38**(8): 3011-3033.
- McNamara, D. D., S. Sewell, E. Buscarlet and I. C. Wallis (2016). "A review of the Rotokawa
- Geothermal Field, New Zealand." Geothermics **59**: 281-293.
- Milicich, S. D., C. Bardsley, G. Bignall and C. J. N. Wilson (2014). "3-D interpretative modelling
- applied to the geology of the Kawerau geothermal system, Taupo Volcanic Zone, New Zealand."
- 843 <u>Geothermics</u> **51**: 344-350.
- Milicich, S. D., I. Chambefort, C. J. N. Wilson, S. Alcaraz, T. R. Ireland, C. Bardsley and M. P.
- Simpson (2020). "A zircon U-Pb geochronology for the Rotokawa geothermal system, New Zealand,
- with implications for Taupō Volcanic Zone evolution." <u>Journal of Volcanology and Geothermal</u>
- 847 Research **389**: 106729.
- Milicich, S. D., C. Massiot and B. Murphy (2023). Fracture permeability in basement greywacke for
- 849 <u>supercritical drilling planning</u>. 45th New Zealand Geothermal Workshop, Auckland, New Zealand.
- Morgenstern, R., N. J. Litchfield, R. M. Langridge, D. W. Heron, D. B. Townsend, P. Villamor, D. J.
- A. Barrell, W. F. Ries, R. J. Van Dissen, K. J. Clark, G. L. Coffey, A. Zoeller, A. Howell and L. H.
- 852 Easterbrook-Clarke (2025). "New Zealand Active Faults Database: the high-resolution dataset v2.0."
- New Zealand Journal of Geology and Geophysics **68**(5): 955-970.
- Mortensen, A. K., Þ. Egilson, B. Gautason, S. Árnadóttir and Á. Guðmundsson (2014). "Stratigraphy,
- alteration mineralogy, permeability and temperature conditions of well IDDP-1, Krafla, NE-Iceland."
- 856 <u>Geothermics</u> **49**: 31-41.

- Mroczek, E. K., S. D. Milicich, P. F. Bixley, F. Sepulveda, E. A. Bertrand, S. Soengkono and A. J. Rae
- 858 (2016). "Ohaaki geothermal system: Refinement of a conceptual reservoir model." Geothermics 59:
- 859 311-324.
- Mroczek, S., M. K. Savage, C. Hopp and S. M. Sewell (2020). "Anisotropy as an indicator for
- reservoir changes: example from the Rotokawa and Ngatamariki geothermal fields, New Zealand."
- 862 Geophysical Journal International **220**(1): 1-17.
- Muraoka, H., T. Uchida, M. Sasada, M. Yagi, K. Akaku, M. Sasaki, K. Yasukawa, S.-i. Miyazaki, N.
- Doi, S. Saito, K. Sato and S. Tanaka (1998). "Deep geothermal resources survey program: igneous,
- metamorphic and hydrothermal processes in a well encountering 500°C at 3729 m depth, kakkonda,
- 866 japan." Geothermics 27(5): 507-534.
- Nemoto, K., N. Watanabe, N. Hirano and N. Tsuchiya (2009). "Direct measurement of contact area
- and stress dependence of anisotropic flow through rock fracture with heterogeneous aperture
- distribution." <u>Earth and Planetary Science Letters</u> **281**(1): 81-87.
- Nicholl, M. J., H. Rajaram, R. J. Glass and R. Detwiler (1999). "Saturated flow in a single fracture:
- evaluation of the Reynolds Equation in measured aperture fields." Water Resources Research **35**(11):
- 872 3361-3373.
- Nicol, A., J. Walsh, K. Berryman and P. Villamor (2006). "Interdependence of fault displacement rates
- and paleoearthquakes in an active rift." Geology 34(10): 865-868.
- O'Sullivan, J., M. Gravatt, J. Riffault, T. Renaud, M. O'Sullivan, N. C. Ruiz, B. Ayling and W.
- Mannington (2025). "An updated model of Ohaaki geothermal field, New Zealand." Geothermics
- **130**: 103339.
- Odoh, I. B. and A. G. Onwuemesi (2009). "Estimation of anisotropic properties of fractures in Presco
- 879 campus of Ebonyi State University Abakaliki, Nigeria using Azimuthal resistivity survey method."
- 380 <u>Journal of Geology and Mining Research</u> 8: 172-179.
- Olsson, W. A. and S. R. Brown (1993). "Hydromechanical response of a fracture undergoing
- compression and shear." <u>International Journal of Rock Mechanics and Mining Sciences &</u>
- 883 Geomechanics Abstracts **30**(7): 845-851.
- Pearson-Grant, S. C. and E. A. Bertrand (2021). "Topography as a Major Influence on Geothermal
- 885 Circulation in the Taupo Volcanic Zone, New Zealand." Geophysical Research Letters 48(8):
- 886 e2020GL092248.
- Rajput, V., E. Kaya, B. Lynne and D. E. Altar (2024). Reactive transport modelling of NCG-
- reinjection at Ngawha geothermal field. 46th New Zealand Geothermal Workshop. Auckland, New
- 889 Zealand.
- Reeves, R. and J. B. Pederson (2023). Insights into the Waiotapu Geothermal Field using high
- resolutions SkyTEM data. New Zealand Geothermal Workshop. 2023.
- Revil, A. and P. W. J. Glover (1998). "Nature of surface electrical conductivity in natural sands,
- sandstones, and clays." <u>Geophysical Research Letters</u> **25**(5): 691-694.
- Robertson, K., S. Thiel and N. Meqbel (2020). "Quality over quantity: on workflow and model space
- exploration of 3D inversion of MT data." <u>Earth, Planets and Space</u> 72(1).
- Rosenberg, M. (2017). Volcanic and tectonic perspectives on the age and evolution of the Wairakei-
- 897 <u>Tauhara geothermal system</u>. PhD, Victoria University of Wellington.
- 898 Rowland, J. V. and S. F. Simmons (2012). "Hydrologic, Magmatic, and Tectonic Controls on
- 899 Hydrothermal Flow, Taupo Volcanic Zone, New Zealand: Implications for the Formation of
- 900 Epithermal Vein Deposits." <u>Economic Geology</u> **107**(3): 427-457.
- Rucker, D. F., J. B. Fink and M. H. Loke (2011). "Environmental monitoring of leaks using time-
- lapsed long electrode electrical resistivity." <u>Journal of Applied Geophysics</u> 74(4): 242-254.

- 903 Sawayama, K., T. Ishibashi, F. Jiang and T. Tsuji (2023). "Relationship Between Permeability and
- 904 Resistivity of Sheared Rock Fractures: The Role of Tortuosity and Flow Path Percolation."
- 905 Geophysical Research Letters **50**(20): e2023GL104418.
- 906 Sawayama, K., T. Ishibashi, F. Jiang, T. Tsuji and Y. Fujimitsu (2021a). "Relating Hydraulic-
- 907 Electrical-Elastic Properties of Natural Rock Fractures at Elevated Stress and Associated Transient
- 908 Changes of Fracture Flow." Rock Mechanics and Rock Engineering 54(5): 2145-2164.
- 909 Sawayama, K., T. Ishibashi, F. Jiang, T. Tsuji, O. Nishizawa and Y. Fujimitsu (2021b). "Scale-
- 910 independent relationship between permeability and resistivity in mated fractures with natural rough
- 911 surfaces." Geothermics **94**: 102065.
- Scott, S., T. Driesner and P. Weis (2016). "The thermal structure and temporal evolution of high-
- enthalpy geothermal systems." Geothermics **62**: 33-47.
- 914 Seebeck, H., A. Nicol, P. Villamor, J. Ristau and J. Pettinga (2014). "Structure and kinematics of the
- 915 Taupo Rift, New Zealand." <u>Tectonics</u> **33**(6): 1178-1199.
- 916 Seebeck, H., R. Van Dissen, N. Litchfield, P. M. Barnes, A. Nicol, R. Langridge, D. J. A. Barrell, P.
- Villamor, S. Ellis, M. Rattenbury, S. Bannister, M. Gerstenberger, F. Ghisetti, R. Sutherland, H.
- 918 Hirschberg, J. Fraser, S. D. Nodder, M. Stirling, J. Humphrey, K. J. Bland, A. Howell, J. Mountjoy, V.
- Moon, T. Stahl, F. Spinardi, D. Townsend, K. Clark, I. Hamling, S. Cox, W. de Lange, P. Wopereis, M.
- Johnston, R. Morgenstern, G. Coffey, J. D. Eccles, T. Little, B. Fry, J. Griffin, J. Townend, N.
- Mortimer, S. Alcaraz, C. Massiot, J. V. Rowland, J. Muirhead, P. Upton and J. Lee (2024). "The New
- 922 Zealand Community Fault Model version 1.0: an improved geological foundation for seismic hazard
- 923 modelling." New Zealand Journal of Geology and Geophysics 67(2): 209-229.
- 924 Sharifzadeh, M., Y. Mitani and T. Esaki (2008). "Rock Joint Surfaces Measurement and Analysis of
- 925 Aperture Distribution under Different Normal and Shear Loading using GIS." Rock Mechanics and
- 926 Rock Engineering 41(2): 299-323.
- 927 Sibson, R. H. (2000). "Fluid involvement in normal faulting." Journal of Geodynamics 29(3): 469-
- 928 499
- 929 Simmons, S. F. and P. R. L. Browne (2000). "Hydrothermal Minerals and Precious Metals in the
- 930 Broadlands-Ohaaki Geothermal System: Implications for Understanding Low-Sulfidation Epithermal
- 931 Environments." Economic Geology **95**(5): 971-999.
- 932 Siratovich, P. A., M. J. Heap, M. C. Villenueve, J. W. Cole and T. Reuschlé (2014). "Physical property
- 933 relationships of the Rotokawa Andesite, a significant geothermal reservoir rock in the Taupo Volcanic
- 2019 Zone, New Zealand." Geothermal Energy 2(1): 10.
- Tateishi, Y., R. Itoi, T. Tanaka and J. Takayama (2015). Natural-state modeling of geothermal
- 936 reservoir at Ogiri, Japan using iTOUGH2. Fortieth workshop on geothermal reservoir engineering.
- 937 Stanford University, Stanford, California.
- 938 Ucok, H., I. Ershaghi and G. R. Olhoeft (1980). "Electrical Resistivity of Geothermal Brines." Journal
- 939 <u>of Petroleum Technology</u> **32**(04): 717-727.
- van Driel, M., T. Renaud, M. Gravatt, M. J. O'Sullivan, J. O'Sullivan, J. Riffault, A. Croucher, F. N.
- van de Vosse and N. Castillo Ruiz (2023). Numerical modelling of tracer tests in the Ohaaki
- geothermal system. 45th New Zealand Geothermal Workshop. Auckland, New Zealand.
- Vidal, J., A. Genter and J. Schmittbuhl (2016). "Pre- and post-stimulation characterization of
- 944 geothermal well GRT-1, Rittershoffen, France: insights from acoustic image logs of hard fractured
- 945 rock." Geophysical Journal International **206**(2): 845-860.
- 946 Villamor, P., K. R. Berryman, S. M. Ellis, G. Schreurs, L. M. Wallace, G. S. Leonard, R. M.
- 947 Langridge and W. F. Ries (2017). "Rapid Evolution of Subduction-Related Continental Intraarc Rifts:
- 948 The Taupo Rift, New Zealand." <u>Tectonics</u> **36**(10): 2250-2272.
- 949 Wallis, I. C. (2023). The Geologic Controls on Geothermal Fluid Flux at the District-, Reservoir-, and
- 950 Wellbore-Scale. PhD, University of Auckland.

- Wallis, I. C., S. McCormick, S. Sewell and C. Boseley (2009). Formation assessment in geothermal
- using wireline tools application and early results from the Ngatamariki geothermal field, New
- 953 Zealand. New Zealand Geothermal Workshop. Rotorua.
- Wallis, I. C., D. D. McNamara, J. V. Rowland and C. Massiot (2012). The nature of fracture
- permeability in the basement greywacke at Kawerau Geothermal Field, New Zealand. Thirty-Seventh
- 956 Workshop on Geothermal Reservoir Engineering. Stanford University Stanford, CA.
- Wang, L., Z.-G. Wu, Y.-R. Fan and L.-Z. Huo (2020). "Fast anisotropic resistivities inversion of
- 958 logging-while-drilling resistivity measurements in high-angle and horizontal wells." Applied
- 959 <u>Geophysics</u> 17(3): 390-400.
- Wannamaker, P. E. (2005). "Anisotropy Versus Heterogeneity in Continental Solid Earth
- 961 Electromagnetic Studies: Fundamental Response Characteristics and Implications for
- Physicochemical State." <u>Surveys in Geophysics</u> **26**(6): 733-765.
- Watanabe, N., N. Hirano and N. Tsuchiya (2008). "Determination of aperture structure and fluid flow
- in a rock fracture by high-resolution numerical modeling on the basis of a flow-through experiment
- under confining pressure." Water Resources Research 44(6).
- Watanabe, N., N. Hirano and N. Tsuchiya (2009). "Diversity of channeling flow in heterogeneous
- aperture distribution inferred from integrated experimental-numerical analysis on flow through shear
- 968 fracture in granite." <u>Journal of Geophysical Research: Solid Earth</u> 114(B4).
- Watanabe, N., T. Mogi, Y. Yamaya, K. Kitamura, H. Asanuma and N. Tsuchiya (2022). "Electrical
- 970 conductivity of H2O-NaCl fluids under supercritical geothermal conditions and implications for deep
- onductors observed by the magnetotelluric method." <u>Geothermics</u> **101**: 102361.
- Wenning, Q. C., C. Madonna, T. Kurotori and R. Pini (2019). "Spatial Mapping of Fracture Aperture
- 973 Changes With Shear Displacement Using X-ray Computerized Tomography." <u>Journal of Geophysical</u>
- 974 <u>Research: Solid Earth</u> **124**(7): 7320-7340.
- Wilson, C. J. N., B. F. Houghton, M. O. McWilliams, M. A. Lanphere, S. D. Weaver and R. M. Briggs
- 976 (1995). "Volcanic and structural evolution of Taupo Volcanic Zone, New Zealand: a review." <u>Journal</u>
- 977 <u>of Volcanology and Geothermal Research</u> **68**(1): 1-28.
- Wilson, C. J. N. and J. V. Rowland (2016). "The volcanic, magmatic and tectonic setting of the Taupo
- Volcanic Zone, New Zealand, reviewed from a geothermal perspective." Geothermics **59**: 168-187.
- 980 World Health Organisation (2023). Guidelines for drinking-water quality: fourth edition incorporating
- 981 the first and second addenda.
- Wyering, L. D., M. C. Villeneuve, I. C. Wallis, P. A. Siratovich, B. M. Kennedy, D. M. Gravley and J.
- 283 L. Cant (2014). "Mechanical and physical properties of hydrothermally altered rocks, Taupo Volcanic
- Zone, New Zealand." <u>Journal of Volcanology and Geothermal Research</u> **288**: 76-93.
- 985 Yamaya, Y., Y. Suzuki, Y. Murata, K. Okamoto, N. Watanabe, H. Asanuma, H. Hase, Y. Ogawa, T.
- 986 Mogi, K. Ishizu and T. Uchida (2022). "3-D resistivity imaging of the supercritical geothermal system
- 987 in the Sengan geothermal region, NE Japan." <u>Geothermics</u> **103**: 102412.
- 988 Yeboah-Forson, A. and D. Whitman (2014). "Electrical Resistivity Characterization of Anisotropy in
- 989 the Biscayne Aquifer." Groundwater **52**(5): 728-736.
- 290 Zhang, Y.-Y., D.-J. Liu, Q.-H. Ai and M.-J. Qin (2014). "3D modeling and inversion of the electrical
- resistivity tomography using steel cased boreholes as long electrodes." <u>Journal of Applied Geophysics</u>
- 992 **109**: 292-300.

# Supplementary information for "Direction-dependent permeability and resistivity of fractured rocks tuned to New Zealand geothermal reservoirs"

This document supplements the main manuscript by providing details on (10) the effect of using different resolution in modelling individual faults, (11) modification of the permeability calculation from (Kirkby et al. 2016), (12) calculation of fault density exponent from field data, (13) calculation of the ratio of faults along vs across the dominant strike direction, and (14).

### 

#### 10. Comparison of different resolutions

To investigate the sensitivity of the models to cell resolution, models with displacement equal to 5 mm and cell size equal to 0.2 mm, 0.5 mm (as used in main paper), and 0.8 mm were run. These demonstrate that the permeabilities and resistivities resolved the different resolutions are essentially the same, and any minor differences in the histograms are likely due to differences due to random seeds.

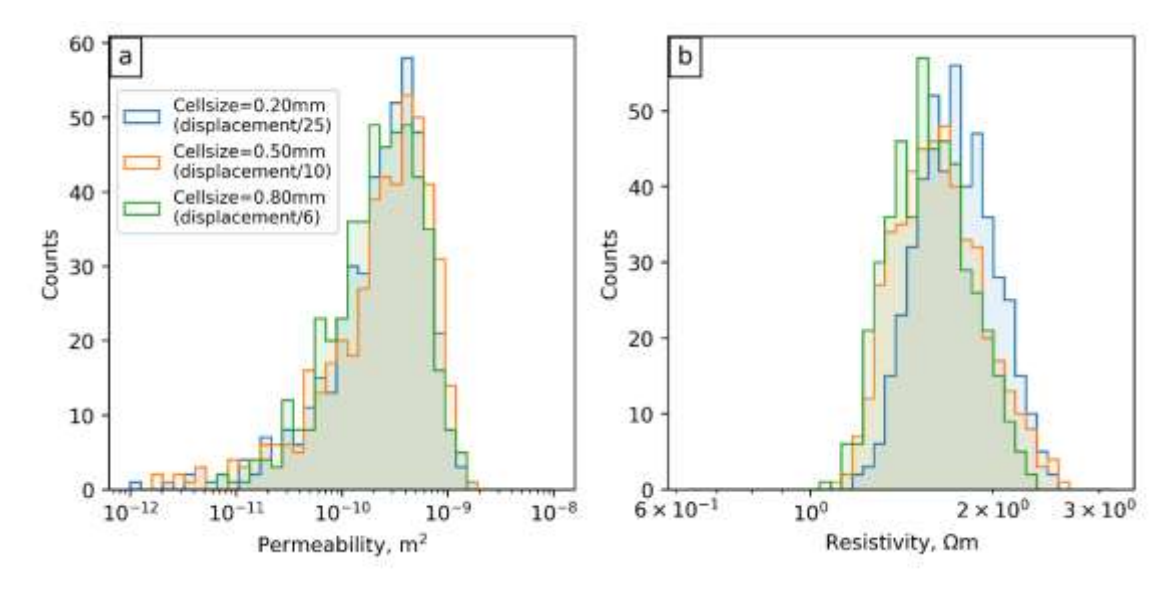


Figure S 1. Fracture model with 5 mm displacement and cell sizes of 0.2, 0.4 and 0.8 mm. a) permeability histogram for models filtered by contact area as in the main paper; b) equivalent resistivity models.

#### 11. Modification to permeability calculation from (Kirkby et al. 2016)

In open parts of the fault, local apertures were corrected to account for the increase in flow path length and variations in aperture associated with non-parallel, sloping plates using a modification of the equation used by Kirkby et al (2016) and Brush & Thomson (2003). The method used by these earlier authors is derived from the analytical solution to Stokes fluid flow in a wedge (Nicholl et al. 1999) but doesn't account for the fact that at large fault separation, the dominant fluid path is likely to become straighter than at low apertures, where fluid is forced to follow the local asperities of the fault plane. The modification in this paper accounts for this and as a result, the permeability of the faults approaches a global parallel plate model at high apertures, as would be expected as the roughness becomes small compared to the aperture.

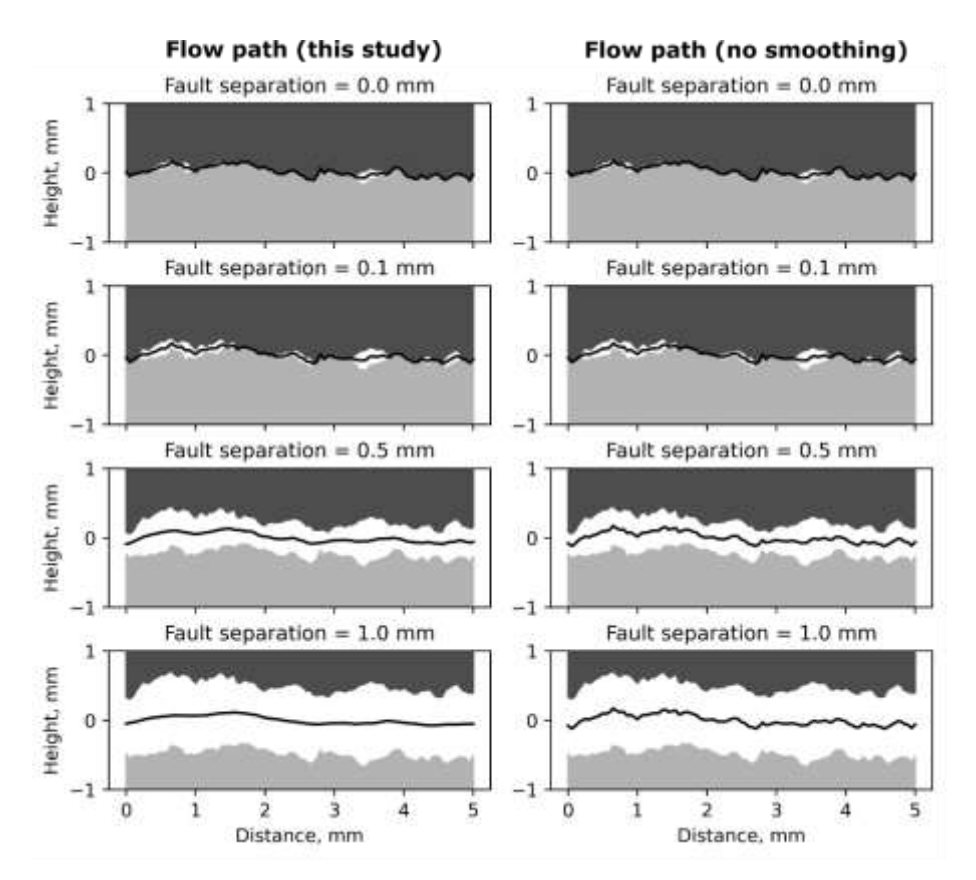


Figure S 2. Modelled flow paths (black lines) between two fault planes in this study (left panel) and previous studies (e.g., Brush and Thomson 2003, Kirkby et al. 2016). At greater fault plane separation, the unsmoothed modelled flow path results in the fluid travelling increased distance and consequently, underestimation of permeability compared to a smoothed flow path.

#### 12. Calculation of fault density exponent

The fault density exponent was fitted using data obtained through mapping of veins in outcrops of basement greywacke rock equivalent to rocks either hosting or underlaying geothermal reservoirs of the Taupō Volcanic Zone (Massiot et al. 2025). Log-log plots of Nf (number of fractures of length >l<sub>min</sub>) as a function of l<sub>min</sub> showed approximately straight-line segments between lengths of 0.4-0.8, and 4.0 m (consistent with truncation limits imposed by the outcrop sizes).

Equation 2 from the main paper (fixing R to 1m such that  $N_f$  is a fault density per  $m^2$ ), can be expressed in log-log space as:

1041 
$$\log(N_f) = \log(\frac{\alpha}{1-\gamma}) + (1-\gamma)\log(l_{min})$$
 (Equation S1)

Fitting a straight line to  $\log(N_f)$  as a function of  $\log(l_{min})$  returns a slope  $(1 - \gamma)$  and intercept  $\log(\frac{\alpha}{1-\gamma})$ .

The slopes, intercepts, and final calculated values of  $\gamma$  (i.e. 2.9 and 3.1 as used in the paper) are listed in Table S1 for truncation lengths of 0.4 and 0.8. Final fits and  $\gamma$  values are also shown in Figure S2.

Dataset	Truncation	Censoring	Slope	Intercept	Gamma
	length	length			
	(minimum),	(maximum),			
	m	m			
Outcrop	0.8	4.0	-2.128	-0.824	3.128
mapping					
Massiot et al					
(2025)					
Active faults	3000	10000	-2.630	3.293	3.630
(Morgenstern					
et al. 2025)					

Table S 1. Truncation and censoring lengths, and fitted slope and intercept of log(Nf) as a function of  $log(l_{min})$ , and gamma values derived from fitting, from outcrop mapping of faults in greywacke (Massiot et al. 2025) and from the NZ active fault database (Morgenstern et al. 2025).

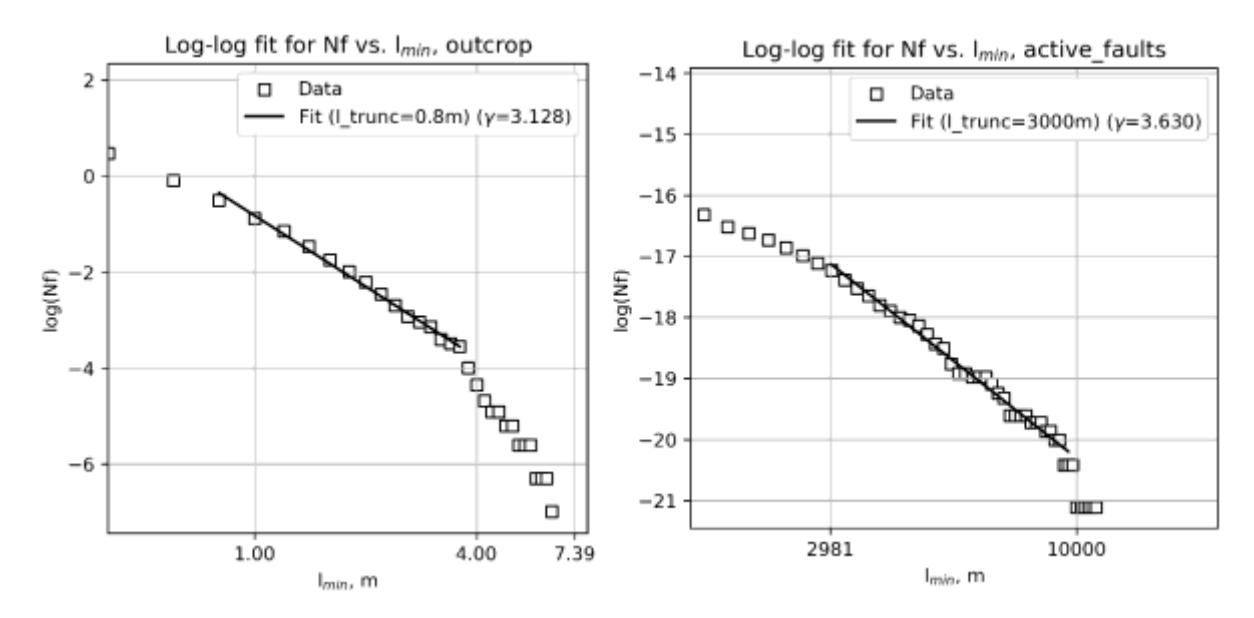


Figure S 3. Number of faults, Nf, as a function of  $l_{min}$ , from veins measured on outcrops of greywacke basement rocks at Awakeri quarry and Rarangi, New Zealand, displayed as a log-log plot. Fitted straight lines (and derived  $\gamma$ ) corresponding to truncation lengths of 0.4 and 0.8 m displayed on the plots.

#### 13. Calculation of ratio of along vs across-strike faults

This section discusses derivation of the parameter  $P_z$ , the proportion of along-strike active faults in the Taupo Rift. Horizontal  $P_z$  was estimated based on a length-weighted average of the strike-parallel component of faults from the Taupo Rift in New Zealand's active fault database (Morgenstern et al. 2025), relative to the total length of faults in this region.

Prior to analysis, the faults were divided into segments with a maximum length of 200 m. We used only segments that fall within the Taupo Rift between the townships of Taupo and Waikite. This limits the complication of the influence of the change in rift axis orientation north of Waikite. (Figure S 4).

1065 
$$P_z = \sum l \cos(\theta - 48.2) / \sum l$$
 (Equation S2)

Where l is the length of each segment ( $\leq 200$  m by definition), theta is the strike of that fault segment in degrees east of north, determined by linear regression of the x, y coordinates of that segment, and 48.2 is the median fault strike (= across all segments within the Taupō Rift. This analysis returned  $P_{along-strike}$  equal to 0.8.

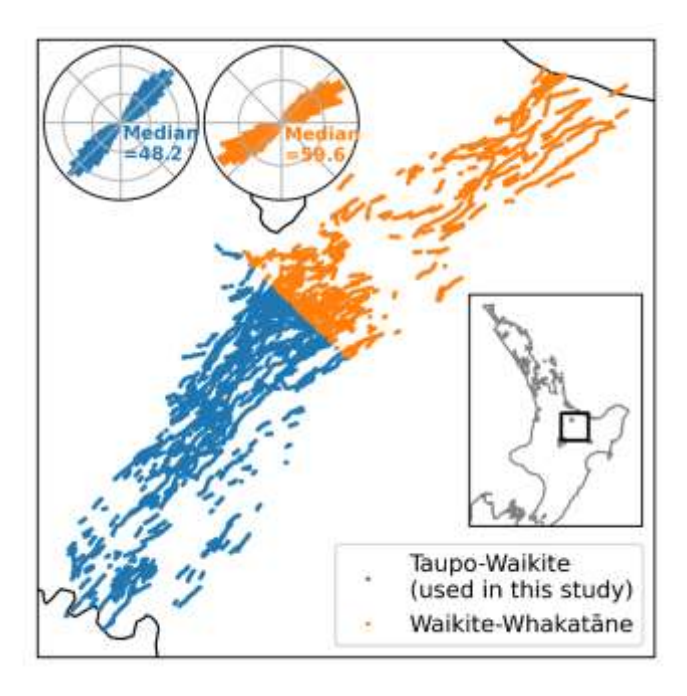


Figure S 4. Centroids of fault segments used for analysis of the proportion of along to across-strike faults in the Taupō Rift. Fault segments are separated into two groups; southern section from Taupō to Waikite Valley (blue) and from Waikite to the coast (orange). Rose diagrams illustrate the distribution of azimuths each part.

1074 A similar analysis was carried out on fracture's dip magntude data interpreted from borehole 1075 images at the Rotokawa and Wairakei geothermal fields (Massiot et al. 2017, McNamara et 1076 al. 2019), i.e.:

 $P_z = \sum l \cos(\theta - 90) / \sum l$  (Equation S3)

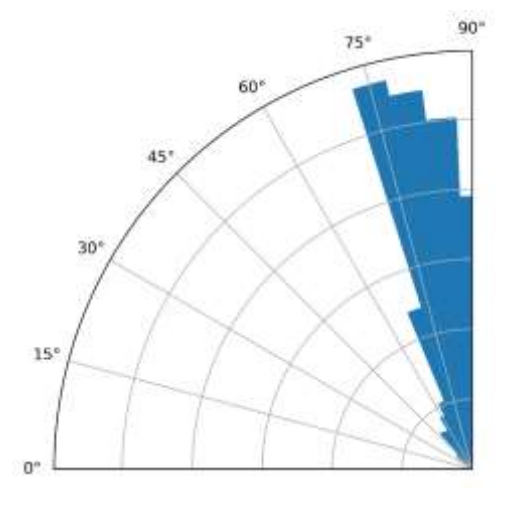


Figure S 5. Dip magnitudes from compiled Rotokawa and Wairakei geothermal fields fracture data interpreted from borehole images (Massiot et al. 2017, McNamara et al. 2019) used for calculation of P<sub>z</sub>, displayed as a rose diagram.

## 14. Fitting of histogram permeability peak as a function of aperture, and aperture as a function of length

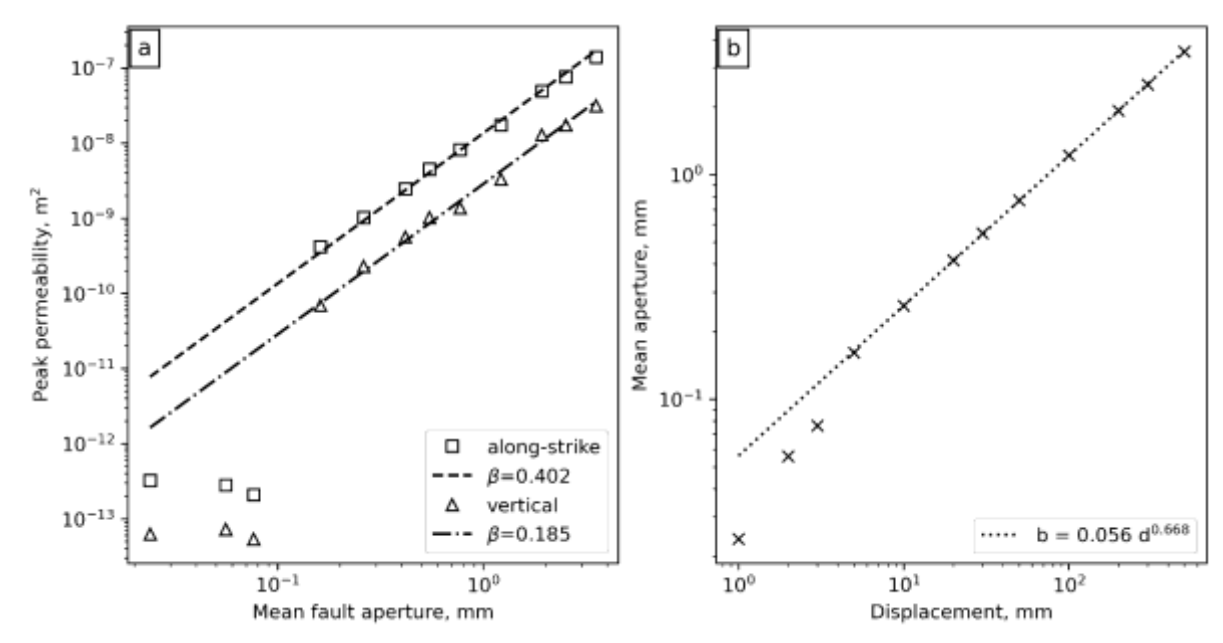


Figure S 6. (a) Peak permeability from Figure 3 as a function of arithmetic mean fault aperture. (b) mean aperture as a function of displacement.

#### 15. References

Brush, D. J. and N. R. Thomson (2003). "Fluid flow in synthetic rough-walled fractures: Navier-Stokes, Stokes, and local cubic law simulations." <u>Water Resources Research</u> **39**(4).

1092 Kirkby, A., G. Heinson and L. Krieger (2016). "Relating permeability and electrical resistivity in fractures using random resistor network models." <u>Journal of Geophysical Research: Solid Earth</u> 1094 **121**(3): 1546-1564.

1095 Massiot, C., M. S. D., J. Siru, M. Nick, M. Regine and I. and Chambefort (2025). "Multi-scale controls on veining in New Zealand greywacke basement rocks: implications for geothermal fluid circulation." 1097 New Zealand Journal of Geology and Geophysics: 1-22.

Massiot, C., A. Nicol, D. D. McNamara and J. Townend (2017). "Evidence for tectonic, lithologic, and thermal controls on fracture system geometries in an andesitic high-temperature geothermal field."

Journal of Geophysical Research: Solid Earth **122**(8): 6853-6874.

McNamara, D. D., S. D. Milicich, C. Massiot, P. Villamor, K. McLean, F. Sépulveda and W. F. Ries (2019).

"Tectonic Controls on Taupo Volcanic Zone Geothermal Expression: Insights From Te Mihi, Wairakei

1103 Geothermal Field." <u>Tectonics</u> **38**(8): 3011-3033.

Morgenstern, R., N. J. Litchfield, R. M. Langridge, D. W. Heron, D. B. Townsend, P. Villamor, D. J. A.
 Barrell, W. F. Ries, R. J. Van Dissen, K. J. Clark, G. L. Coffey, A. Zoeller, A. Howell and L. H. Easterbrook-Clarke (2025). "New Zealand Active Faults Database: the high-resolution dataset v2.0." <a href="New Zealand">New Zealand</a>
 Journal of Geology and Geophysics 68(5): 955-970.

Nicholl, M. J., H. Rajaram, R. J. Glass and R. Detwiler (1999). "Saturated flow in a single fracture:

evaluation of the Reynolds Equation in measured aperture fields." <u>Water Resources Research</u> **35**(11): 3361-3373.

1111

1082

1083

1084

1085 1086 1087

1088